Enhanced Lithological Mapping in El-Missikat and El-Erediya Areas, Central Eastern Desert, Egypt, Leveraging Remote Sensing Techniques and Machine Learning Algorithms

Aya S. Shereif, Ali Shebl, Abdelhalim Shokry Mahmoud, and Árpád Csámer

***Abstract*— In the field of mineral exploration, it is strikingly evident that radioactive-bearing mineralization predominantly resides within granitic intrusions and along structural discontinuities. Consequently, the comprehensive mapping of lithological features emerges as a crucial means of accurately guiding the identification of these mineralizations. The present research is dedicated to enhancing the characterization of granitic rocks located within Egypt's Central Eastern Desert (El-Missikat and El-Erediya regions). These areas have garnered attention due to their notably high concentrations of radioactive mineralizations, prompting the need for a more in-depth investigation. Despite the study area's importance for potential radioactive mineral deposits, examining the geological map reveals notable challenges and inconveniences. Our research aims to address these issues using remote sensing data and machine learning algorithms (MLAs). We used image processing techniques, including false-color composites (FCCs), principal component analysis (PCA), and independent component analysis (ICA) to identify eight lithological targets and generate reference maps for the study area.The widely used support vector machine (SVM) was trained with informative image combinations, showing reasonable lithological allocations, especially when it fed with FCC 12-6-2 in RGB. Our study found that incorporating dimensionality-reduction techniques like PCA and ICA with FCCs significantly boosted accuracy by over 15%. Using Sentinel-2 imagery and SVM, we created a novel lithological map for the challenging study area, pinpointing mineralization-rich zones, particularly those linked to shear zones within granitic rocks. This map enhances progress in characterizing rock units, and we strongly advocate the use of dimensionality-reduction techniques, such as PCA and ICA, to feed MLAs. These techniques play a crucial role in producing precise, unbiased lithological maps for complex terrains, aiding in the localization of valuable mineral deposits.**

Received 11 February 2024; revised 5 July 2024; accepted 7 September 2024. Date of publication 3 October 2024; date of current version 24 October 2024. The work of Aya S. Shereif and Ali Shebl was supported by the Stipendium Hungaricum Scholarship under the Joint Executive Program between Hungary and Egypt. *(All the authors contributed equally to this work.) (Corresponding author: Árpád Csámer.)*

Aya S. Shereif and Ali Shebl are with the Department of Geology, Faculty of Science, Tanta University, Tanta 31527, Egypt, and also with the Department of Mineralogy and Geology, University of Debrecen, 4032 Debrecen, Hungary (e-mail: aya.salah@science.tanta.edu.eg; ali.shebl@science.tanta.edu.eg).

Abdelhalim Shokry Mahmoud is with the Department of Geology, Fayoum University, Al-Fayoum 63514, Egypt (e-mail: asm07@fayoum.edu.eg).

Árpád Csámer is with the Department of Mineralogy and Geology and the Cosmochemistry and Cosmic Methods Research Group, University of Debrecen, 4032 Debrecen, Hungary (e-mail: csamera@unideb.hu).

Digital Object Identifier 10.1109/TGRS.2024.3471982

***Index Terms*— Arabian–Nubian shield (ANS) and Eastern Desert, geological mapping, mineralized shear zones, Sentinel 2, support vector machine (SVM).**

I. Introduction

LITHOLOGICAL mapping plays a crucial role in mineral exploration, efficient geological surveys [1], [2], [3], [4], [5], [6] analyzing numerous environmental hazards, and planning land use [7], [8], [9]. This is mainly attributed to the encapsulation of basic information about the accurate identification of host rocks that in turn could facilitate a better understanding of a considered area. The reliable and efficient outputs of lithological mapping substantially contribute to mineralization identification and other several natural resources besides better planning for natural hazard mitigation.

As a consequence of the importance of accurate lithological mapping, several techniques have recently been implemented for developing the mapping process and increasing the reliability of the outputs. For instance, remote sensing data and geophysical methods (airborne gamma-ray spectrometric data and aeromagnetic data) with the aid of geological and geochemical data were applied [10], [11]. Lithological mapping and identifying the contacts between different lithologies by using airborne gamma-ray spectrometric data is premised essentially on the measurements of the varied concentrations of K, Th, and U in these rock units because this way offers a means of identifying geochemical fluctuations in (K, Th, and U) to each rock units from the Earth's surface [12]. However, insufficient geochemical data or the unavailability of geophysical surveys pose a challenge to the optimization of lithological mapping efficiency, particularly in intricate regions, inaccessible lands, and rugged terrains [13]. Consequently, remote sensing data have been increasingly utilized in the last two decades in lithological mapping [4], [14], [15], [16], [17], [18], [19], [20].

The number of studies that used remote sensing datasets (e.g., ALI, ASTER, Landsat, and S2) for solving geological complexity in several terrains, highlighted the importance of these images as a tool in geological investigations. Thus, it is widely accepted as an alternative and cost-effective, readily accessible, and rapid asset for conducting lithological

mapping. It depends mainly on highlighting the spectral responses (that depend on the physical and chemical properties of rocks) and texture information of the various rock units [21], [22], [23], [24], and providing significant information for mineral exploration [25]. In addition to time and effort savings, they produce precise and effective mapping outcomes, particularly in areas that are difficult to access for conventional fieldwork [6]. The reliable outputs of lithological mapping by remote sensing datasets and digital image processing techniques are considered one way to track the mineralization [26], [27], [28].

Among various available remote sensing datasets, the current research depends mainly on Sentinel-2 data. The latter is considered one of the best optical satellites in terms of pixel size (10 m) and data availability (free access). In addition, it provides advanced spectral resolution through its 13 channels distributed across the visible near-infrared (VNIR) and short-wave infrared (SWIR). These spectral and spatial configurations are effectively utilized for enhanced mineralogical and lithological identification [18].

What has greatly bolstered the optimal utilization of remote sensing data while emphasizing their efficiency is the seamless integration with machine learning algorithms (MLAs) which are considered a subdomain of artificial intelligence (AI). Particularly with the presence of various MLAs and the availability of remote sensing datasets in the field of geosciences, as highlighted by numerous authors [10], [18], [29]. MLAs leverage computational techniques through statistical or nonprobabilistic approaches to recognize patterns and relationships within geological datasets [30], aiding in the identification and classification of lithological units by large numbers of pixels that can be classified based on smaller numbers of labeled pixels, generally referred to as training data [6]. In addition, the primary advantage of MLAs lies in their capacity to address intricate nonlinear mappings, their ability to leverage substantial volumes of data without presuming data distribution, and their capability to incorporate additional datasets to enhance class separability and classification [31].

Expanding upon those mentioned above, in the last two decades machine learning techniques have found extensive application in addressing scientific and engineering challenges [32], [33], [34]. The use of MLAs (e.g., random forest (RF), support vector machine (SVM), logistic regression, and deep learning algorithms) in geological processes, especially in lithological mapping and mineral prospectively mapping has become increasingly prevalent and garnered interest, due to their capacity to improve geological analyses. Various MLAs have been extensively utilized to achieve precise lithological classifications. These utilized MLAs can be broadly categorized into parametric types such as maximum likelihood classifier (MLC), being a representative example, especially suitable for normally distributed [35].

In addition, there are nonparametric types such as artificial neural networks (ANNs) [36], RFs [37], [38], k-nearest neighbors (K-NNs) [39], and SVM methods [38], [40], these nonparametric classifiers are efficiently employed in lithological mapping using remote sensing data. SVM is considered a supervised MLA, a well-known efficient classifier, frequently endorsed, widely applied in numerous studies, and stands out as one of the most potent and favored algorithms in performing lithological mapping due to their capacity to establish nonlinear decision boundaries within a high-dimensional feature space by the aid of geological and geophysical data [25], [41], [42], [43].

The current research is an attempt to make the best use of MLAs and remote sensing data to decipher the geological complexity of the study area (El-Missikat and El-Erediya). The latter is situated in the Central Eastern Desert of Egypt and contains significant radioactive uranium–thorium (U–Th) mineral deposits accompanied by other nonradioactive mineralization, such as silver (Ag), fluorine (F), and molybdenum (Mo) [44]. It is recognized as the foremost uranium occurrence in the Eastern Desert of Egypt, they are also classified as uraniferous granites [45], [46], [47], [48], [49]. Due to the economic importance of these deposits, the study area attracted the attention of many researchers and geologists performing several geological investigations [45], [46], [47], [50], [51], [52], [53], [54], [55], [56], [57], [58], [59], [60], [61] and there are many geological maps [47], [57], [58], [62], [63], [64], [65] that have been implemented for the considered area. Notwithstanding the foregoing, we noticed considered variations and discrepancies among these maps [62], [66], [67], [68] and this heightened our motivation to discern the distinctions among these geological maps and recreate a new lithological map for the study area utilizing remote sensing data and SVM to ensure the objectivity of our output.

Consequently, the current study aims to answer why such variations exist despite the consistent study area by minimizing subjectivity that might have influenced previous maps. By leveraging MLAs, renowned for their objectivity and accuracy, we integrated high-resolution remote sensing data (Sentinel-2) with SVMs. In addition, our research aims at enhancing the localization of mineralization especially radioactive mineralization through accurate detection of the shear zones within the study area which are considered the main host for mineralization within the studied terrain.

II. Study Area and Geological Setting

A. Regional Geology

The mainly Neoproterozoic Arabian–Nubian shield (ANS) is located along both sides of the Red Sea, creating one of the largest exposed areas of Precambrian continental crust on Earth [15], [69]. The rocks of ANS found in the Eastern Desert and the Sinai Peninsula, Egypt, constitute the northern part of the Nubian shield called the Precambrian basement [70] as shown in Fig. 1. Granitic rocks make up approximately 60% of the Neoproterozoic of the northern ANS, which includes northwestern Saudi Arabia, Sudan, Sinai, and the Eastern Desert of Egypt, as reported by [71]. The granitic rocks in Egypt are typically divided into two primary groups, syn- to late-orogenic older gray granitoids (750–610 Ma), and post to anorogenic younger granitoids (YGs) (610–580 Ma) [71], [72], [73], [74], [75], the later ones primarily consist

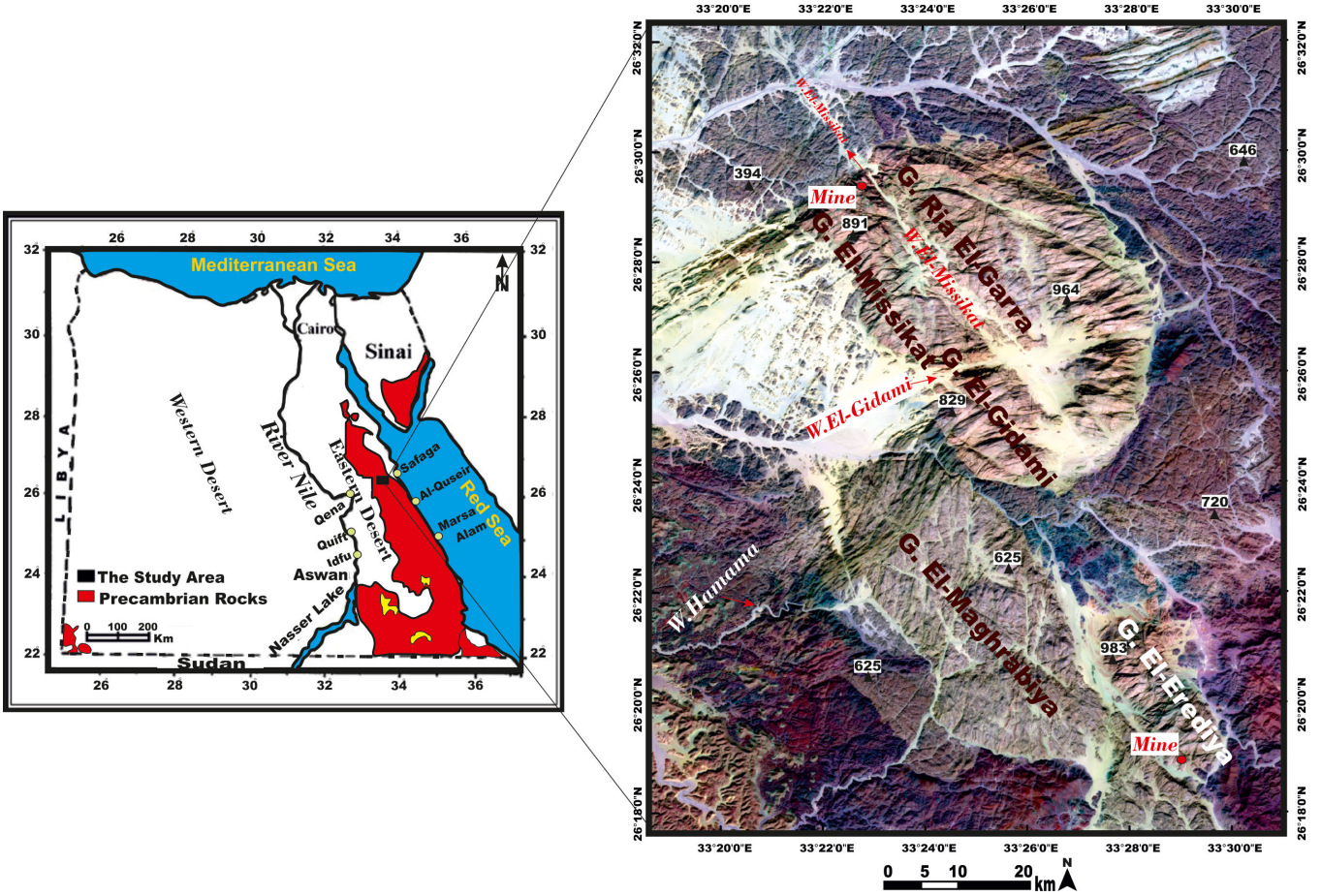

Fig. 1. Location map of El-Missikat-El-Erediya areas, Eastern Desert, Egypt.

of monzogranites (MGs), syenogranites (SGs), and alkali-feldspar granites. These YGs originated during an extensional tectonic process, and they are prevalent throughout the Egyptian shield and are significant sources of mineralizations especially, radioactive ones. The YGs comprise approximately one-third of the plutonic assemblage in the Egyptian shield based on our surveying. A substantial portion of the radioactive anomalies are linked to certain granites, primarily because they host particularly intriguing uranium mineralization. Most late-stage, highly fractionated granites, renowned for their diverse geological formations, are widely acknowledged as exceptionally favorable host rocks for uranium mineralization on a global scale, this recognition is particularly prominent in the case of peraluminous two-mica granites [76], [77], [78].

B. Geological Setting of the Study Area

The study area is situated in the Central Eastern Desert of Egypt and covers about 576 km^2 as it appears in Fig. 1. This area is located between latitudes 26° 18′ and 26° 32′ N, and longitudes 33° 20′ and 33° 30′ E, approximately midway between Qena in the Nile Valley and Safaga on the Red Sea shore (south of Qena and Safaga road), spanning a distance of about 85 km [79]. It includes several well-known areas represented by 1) G. El-Missikat, which was mapped previously as either MGs [80], or SGs [61] or MGs, SGs with altered rich quartz granites [81] and MGs to SGs [82]; 2) G. Ria El-Garra, which represents the eastern side of the study area and parallel to G. El-Missikat and mapped previously as SGs [62]; 3) G. El-Gidami, which is situated in the western part of the region and represents the southwest part of G. El-Missikat and the northern eastern part of G. El-Maghrabiya and mapped previously as SGs [62] and MGs to SGs [82]; 4) G. El-Maghrabiya MGs [67], [82] that is revealed in the western part from G. El-Missikat; and finally 5) G. El-Erediya which is mapped before as SGs [62] and MGs to SGs [82] and it is located in the southern part of G. El-Missikat and in the southeastern part from G. El-Maghrabiya and G. El-Gidami.

The areas of El-Missikat and El-Erediya are distinguished by their wealth of valuable mineralization reserves. These deposits include significant sulfides such as galena, pyrite, chalcopyrite, sphalerite, and molybdenite, as well as barite, fluorite, copper, silver, and gold [44], [83]. It's worth noting that these two granitoid plutons are recognized for their uranium mineralization (primary and secondary), based on our prior knowledge [84], [85], [86], [87].

As they represent the most promising prospects for uranium they captured the attention of onlookers to dig several exploratory mining tunnels through the NW part of G. El-Missikat pluton and the southern part of G. El-Erediya pluton [57], [64], [81], [88], [89], [90], [91]. Besides these granitic plutons, a wide range of other Precambrian and

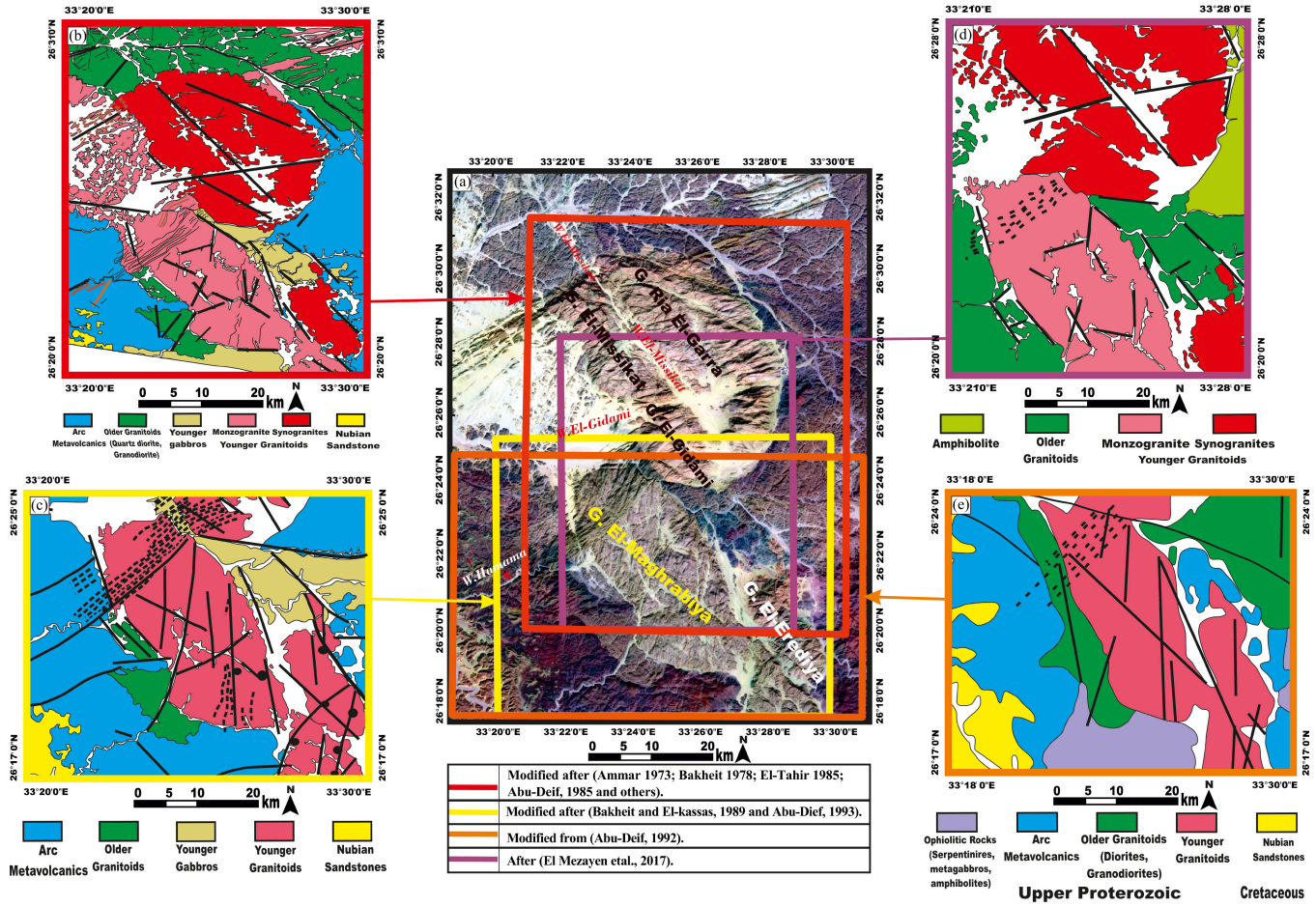

Fig. 2. (a) Overview of the study area through an FCC 12-6-2 in RGB, respectively, featuring the earlier research of various authors. (b) Geological map of El-Missikat-El-Erediya areas (red frame), adapted from previous works [1] and modified after (Ammar, 1973; Bakhit, 1978; Abu-Deif, 1985; El-Tahir, 1985; and others). (c) Geological map of El-Erediya area (yellow frame), adapted from the research of [6] and modified after [7] and [8]. (d) Geological map of El-Erediya area as per [9], and (e) (orange frame) geological map of El-Erediya area, sourced from [10] and modified after (Abu-Deif, 1992). We tried to unify the color representation of each rock unit to facilitate more straightforward comparisons.

Phanerozoic formations are exposed within the study area as depicted in Fig. 2.

The investigated area of study is covered by Neoproterozoic rocks as illustrated in Fig. 2, that belong to the ANS, from oldest to youngest as follows, ophiolitic rocks (serpentinites, amphibolite, metagabbros, and metasediments), island arc metavolcanics (AMVs), syn-tectonic older granitoids (OGs) (diorite, granodiorite, tonalities, and quartz diorite), younger gabbro and posttectonic YGs (MGs, SGs and altered rich quartz granites) as depicted in Fig. 2. All these Precambrian rock units are unconformably overlain to the west by the Early Cretaceous Nubian sandstone (NSS) [62], [66], [67], [68], [81], [82], [92], [93], [94].

The YGs plutons of El-Missikat and El-Erediya are characterized by elevated levels of SiO_2 (more than 73%), total alkalis, metalumonous to slightly peraluminous, low Fe_2O_3, MgO, and TiO_2 [95], exhibit leucocratic characteristics, significant differentiation, and they are accompanied by accessories such as zircon, monazite, fluorite, iron oxides, and apatite [64], [89], [96]. These plutons have formed in a postorogenic event, within the Earth's crust, specifically in a within-plate setting [51], [94]. Significant numbers of geological maps have been produced in the surveyed area [47], [57], [58], [62], [63], [64], [65] and will be summarized below to highlight the main characteristics of each rock unit.

Granitic rocks within the study area can be mainly divided into OGs, MGs, and SGs.

Syn-tectonic OGs also known as quartz diorite [81], [93], diorites [67], tonalities, and granodiorite [67], [81], [93], represent a massive pluton that extended westward and northward beyond the study area. Their age is approximately from 930 to 850 Ma according to [97] and [98], to 711 Ma, as suggested by [99]. Posttectonic YGs had also intruded into the OGs [81]. The OGs are commonly found as low to moderately relief rocks with oriented features and a gneiss-like texture. In certain instances, they may appear as migmatized rocks with distinct alternating dark and white bands [81] and are distinguished by their gray.

Based on their mineral composition, **quartz diorite** is composed essentially of plagioclase (38%), quartz (8%), and K-feldspars (2%) as felsic, and hornblende (18%), augite (13%), and biotite (12%) as mafic minerals. **Granodiorite** consists mainly of quartz (39%), plagioclase (39%), and K-feldspars (varying from 6% to 12%) as rock-forming felsic,

and biotite (13%) and hornblende (1%) as mafic minerals. **Tonalites** are composed essentially of quartz (up to 38%), plagioclase (up to 58%), and K-feldspars (varying from 6% to 12%) as essential felsic, and biotite (20%) and hornblende (1%), as essential mafic minerals [81]. Chlorite, epidote, sericite, and kaolinite are present as alteration products of hornblende and plagioclase. Apatite, zircon, titanite, and rutile are observed as accessory minerals [67].

El-Missikat posttectonic YG (SG), is an oval-shaped pluton (approximately 12-km long and 20-km wide) elongated in the N–S direction and constitutes a moderate to high SG pluton [62], [68]. It exhibits a pink to red and is characterized by a medium to coarse-grained texture displaying a hypidiomorphic texture and dappled with some milky white plagioclase feldspars and grains of smoky quartz. Petrographically, it is composed mainly of quartz, alkali feldspar (mainly perthite and microcline perthites), sodic plagioclase (oligoclase and albite), biotite and muscovite, as essential minerals, apatite, sphene, ilmenite, fluorite, rutile, magnetite, tantalum-bearing minerals and zircon and iron oxides that occur as clots of hematite and limonite as accessory minerals [88], [100]. Uranothorite, xenotime, uraninite, allanite, and monazite also appear rarely [101], [102], [103]. El-Missikat SG is categorized as high potassium calc-alkaline zoned plutons [62], [102].

El-Missikat SG was emplaced during the posttectonic event of the ANS evolution and has been dated to approximately 568 ± 17 Ma according to [104] using the Rb/Sr aging method. Greenberg [99] places their age within the range of 603–575 Ma. For the age determinations for Rie El-Garra, which represents the eastern lobe of the El Missikat granitic mass, Fullagar [104] was reported to be approximately 568 and 570 Ma. The more recent granitoids intrude the syn-tectonic older ones along several hundreds of meters (500–750 m), directly at the northern, western, and eastern parts, exhibiting a distinct sharp contact.

Notably, the El-Missikat SG displays distinct intrusive contacts as it penetrates the adjacent older rocks in the study area. This results in noticeable oval-shaped, dark-colored xenoliths from the older rocks, especially the OGs, being evident within the younger ones. In addition, pegmatites were found in the shape of small lenses, vein-like bodies, zoned and unzoned oval-shaped bodies, and sheets, particularly near the contacts with the OGs [81], [88]. These pegmatites mainly consist of quartz and K-feldspars, with minor amounts of iron oxy-hydroxides, mica, green to violet fluorite, and jasper [93].

El-Erediya posttectonic YGs, are mostly classified as SGs and MGs and are situated in the southeastern region of the mapped area. They display hues ranging from pink to reddish-pink, oval-shaped, and elongated intrusion outlines (NW directions). They possess a slightly leucocratic nature, exhibit a medium to coarse-grained texture with low to moderate relief, and typically reveal a hypidiomorphic texture. It exhibits extensively weathered, exfoliated, and jointed surfaces resulting from weathering processes [105]. They are mainly composed of K-feldspar (31%–34%) (microcline, microcline perthites, orthoclase, and perthite), quartz (30%–35%), and plagioclase (31%–35%) as essential felsic minerals, micas (biotite and muscovite) as essential mafic minerals [67]. Zircon, apatite, fluorite, and Fe-Ti oxides appear as accessory constituents. According to the results of the geochemical analyses the El-Erediya granites are enriched in Nb, Rb, Y, and U but depleted in Ba, Pb, Sr, Zn, and Zr [58], [59]. El-Erediya granitic pluton was emplaced during a posttectonic event of the ANS evolution (ages of 570 ± 5 Ma) [104].

These granitic bodies are dissected by several structural features. NE-SW oriented syn-tectonic felsite dyke swarms cut only the OGs at the northwestern boundary of the El-Missikat-El-Gidami granitic plutons [100]. The northwestern part of El-Missikat YG is intruded by thick aplite dike [103], [106] and traversed by some NW-SE faults and a mineralized shear zone with an NE-SW direction. The El-Erediya YG is intersected by two main fault orientations, with one trending in the northwest to southeast (NW-SE) direction and the other in the north to south (N–S) direction and from the southern part revealed that this pluton is cut by thick aplite dyke.

Shear zones are also prevalent within the study area and have economic importance, several subparallel shear zones, aligned in the northeast-southwest direction intersect the northern part of the El-Missikat pluton, particularly along its interface with OGs in the western part and extend to the north-eastwards in G. El- Garra [107]. Likewise, in the southern sector of the El-Erediya pluton, these shear zones are conspicuous, especially in the proximity of contact with AMV rocks [53]. This is exemplified by tabular and elongated granites that have been subjected to northeast-southwest compression and brecciation, with parallel fractures and joints extending over a distance of 2 km in length and 4 km in width. Furthermore, within this shear zone, multiple generations of quartz (siliceous) veins and veinlets, ranging from 1 to 3 m in thickness, extend for over 2 km [106].

For the El-Missikat area uranium mineralizations are predominantly structure-controlled, primarily concentrated along shear zones especially associated with black and jasperoid silica veins which occur within shear zones [45], [57], [64], [108]. While uranium-bearing mineralizations in the El-Erediya area are always associated with sheared-granite zones, these zones are predominantly situated along the NW-SE and N–E fault systems [66], [109] and this area also has shear zones (ENE-WSW) filled with red and black silicified veins containing many radioactive anomalies with visible yellow secondary uranium minerals [95], [105], [110].

III. Materials and Methods

A. Remote Sensing Data (Sentinel-2)

The European Space Agency (ESA) with the corporation European Commission (EC) launched the Sentinel-2 satellite that carries a single Multispectral Instrument (MSI). Sentinel-2 consists of a pair of identical satellites (A and B) that share the same sun-synchronous orbit and they are positioned with a 180° phase difference from each other. Sentinel-2A and Sentinel-2B were launched on June 23, 2015 and March 7, 2017, respectively, and the cooperation of those twin satellites provides a reasonable temporal resolution of five days [39]. The primary focus of the Sentinel-2 mission is on land cover

TABLE I
CHARACTERISTICS OF SENTINAL-2 DATA

Band Name (b)	Spatial Resolution /Pixel size (m)	Spectral region	Central Wavelength		Band Width (nm)	Purpose
			(µm)	(nm)		
B01	60	Ultra blue	0.443	443	20	Aerosol detection
B02	10	Blue	0.490	490	65	Blue
B03	10	Green	0.560	560	35	Green
B04	10	Red	0.665	665	30	Red
B05	20	VNIR	0.704	704	15	Vegetation Classification
B06	20	VNIR	0.740	740	15	Vegetation Classification
B07	20	VNIR	0.782	782	20	Vegetation Classification
B08	10	VNIR	0.842	842	115	Near-infrared
B08a	20	VNIR narrow	0.865	865	20	Vegetation Classification
B09	60	SWIR (WV)	0.945	945	20	Water Vapor
B10	60	SWIR cirrus	1.375	1375	30	Cirrus
B11	20	SWIR	1.610	1610	90	Snow/Ice/Cloud discrimination
B12	20	SWIR	2.190	2190	180	Snow/Ice/Cloud discrimination

VNIR = visible near-infrared, **SWIR** = short wave infrared.

applications and related tasks in change detection mapping. Sentinel-2 satellite serves as a significant means of monitoring and improving the consistency of Earth observation data with a short revisiting time. It offers adequate spectral coverage (13 spectral bands from 0.433 to 2.280 with a scan width of 290 km) with a spatial resolution of 10–60 m [111] (see Table I).

Sentinel-2 data were preprocessed to the Zone 36 North Universal Transverse Mercator (UTM) projection with the WGS-84 datum, subsequently atmospherically corrected to obtain the surface reflectance using the sen2cor processor within the Sentinel Application Platform (SNAP). Sentinel-2 has proven its efficiency in many geological applications and is adequate for investigations [11], [112], [113], [114], [115], [116], [117], [118], [119], [120], [121], [122], [123], [124].

B. Image Processing Techniques

In the present research, a diverse range of image processing techniques has been harnessed to elevate the quality and information content of the imagery. These methods encompass principal component analysis (PCA), independent component analysis (ICA), false-color composites (FCCs), and decorrelation stretch (DS) per the depiction in Fig. 3. All of these processing techniques were performed using version 5.6.2 of the Environment for Visualizing Images (ENVI) software, (https://www.l3harrisgeospatial.com/SoftwareTechnology/ENVI). Their collective purpose is to substantially enhance the visual representation of the data and more importantly to sharpen the distinction between lithological units while accentuating the delineation of lithological boundaries. The whole adopted methodology is shown in as shown in Fig. 3.

1) False-Color Composites: FCC is a standard RGB representation of three bands (using any combination except for the true-color composite). In geological applications, the choice of bands primarily relies on their capacity to highlight the lithological features based on their spectral characteristics [20], [121], [122]. By combining specific bands after trying to select the best color composite, it becomes significantly more

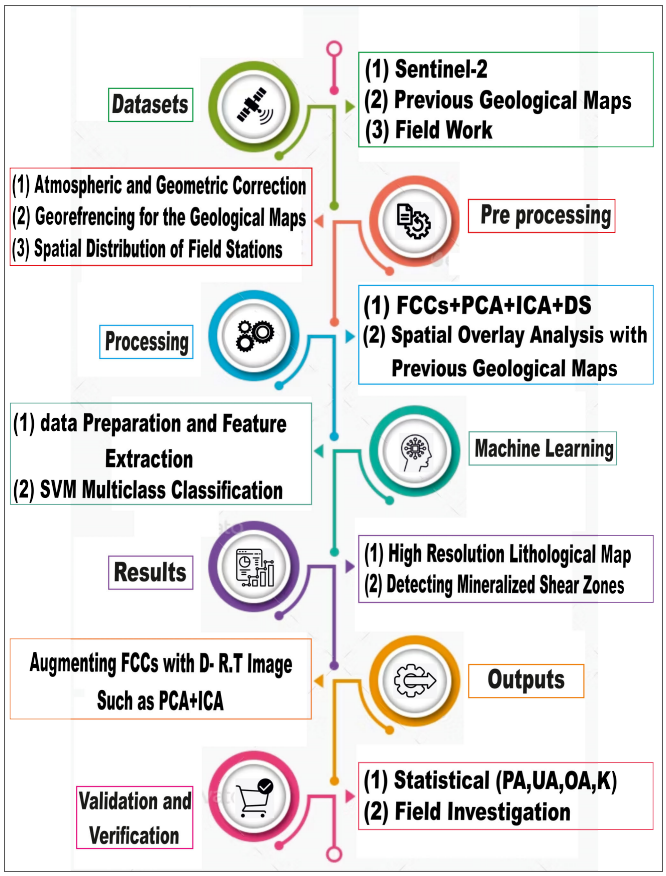

Fig. 3. Flowchart illustrating the methodology employed in the present study.

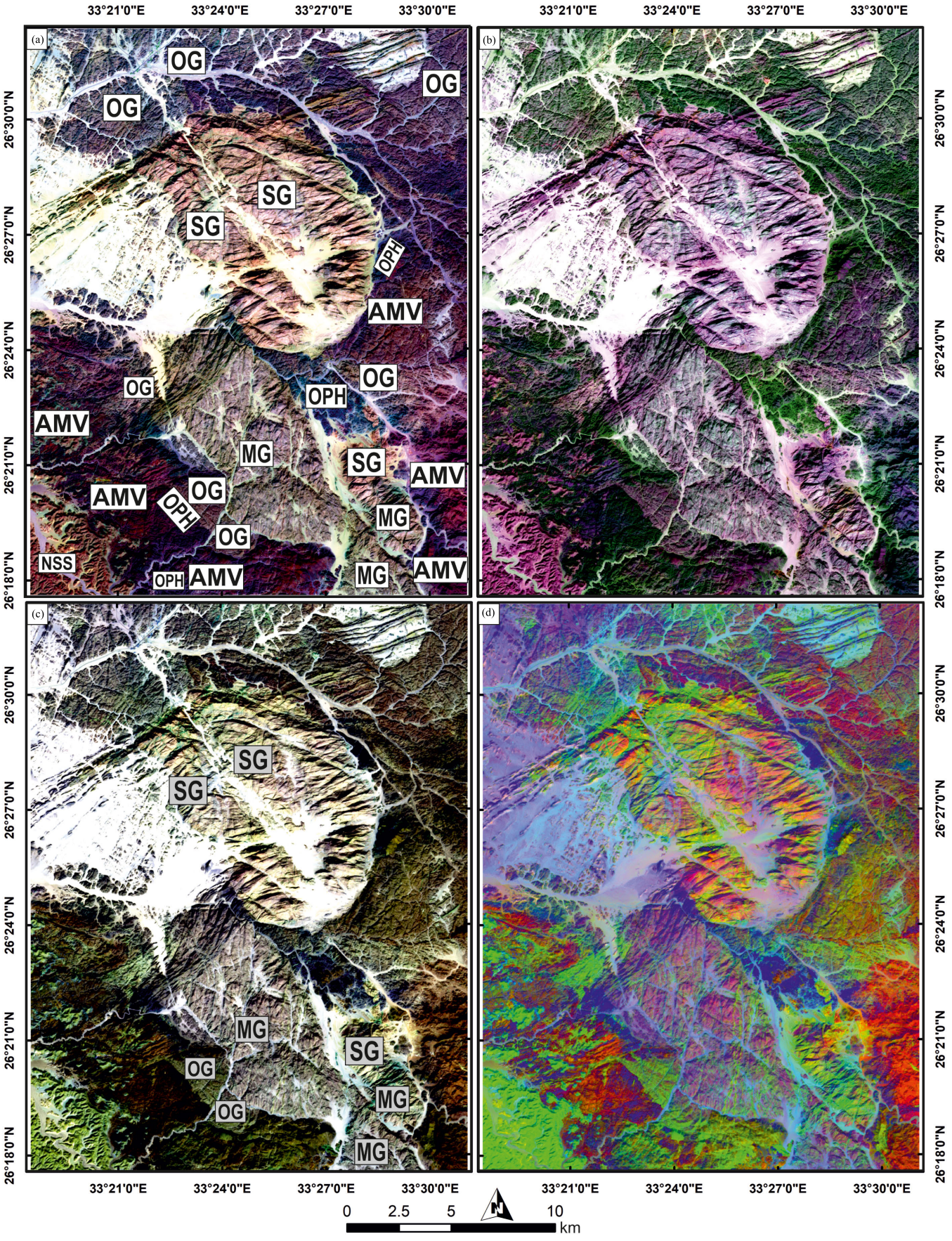

Fig. 4. (a) Lithological discrimination using Sentinel-2 FCCs 12-6-2 in RGB, (b) FCCs 11-2-12 in RGB, and (c) FCCs 12-11-7 in RGB channels. (d) Lithological characterization using DS color composites, DS 12-11-7 in RGB channels.

effective in identifying differences. Several FCCs were applied in this study to discriminate the rock units in the study area, including the combinations 12-6-2, 11-2-12, and 12-11-7 in the RGB channels. The first FCC, 12-6-2 [see Fig. 4(a)], was effective in differentiating the felsic granitoids from the mafic rocks, such as ophiolites (OPHs) and AMVs. In addition, the FCC 11-2-12 in the RGB channels [see Fig. 4(b)] significantly highlighted the shear zones in the study area, including the Northern G. El-Missikat, Northern G. El-Maghrabiya, and Southern G. El-Erediya. Finally, the FCC 12-11-7 in the RGB channels [see Fig. 4(c)] differentiated not only between the felsic granitoid units and mafic rocks but also among various types of granitoid rocks, including OGs, MGs, and SGs, within the study area.

2) Decorrelation Stretch: DS is particularly useful for highlighting subtle variations and details in the data. It depends on manipulating the primary components of the acquired data to produce a color composite image through the removal of interchannel correlation with each pixel [4], [123]. DS is used to enhance the color differences in any false-color combination of satellite images. DS has proven its efficiency in distinguishing rocks [124], [125]. Thus, we applied it as a tool to discriminate between different lithological units in the study area as illustrated in Fig. 4(d).

3) Principal Components (PCs) Analysis: PCA is a dimensionality-reduction mathematical method applied to handle correlated information often associated with remote sensing data. PCA belongs to a category of multidimensional descriptive techniques known as factorial methods [126]. It is also utilized to gather data on characteristics to enhance the targeted information in the image. This can be achieved by converting a set of interrelated variables into several independent and uncorrelated linear variables through the identification of the primary axes in the original data responsible for the most variation. These linear variables carry informative data related to the spectral attributes anticipated from the particular spectral bands in the VNIR and SWIR regions. This is done through an orthogonal transformation known as PCs [112], [113], [114].

Nonetheless, while PCA is highly effective in reducing the dimensionality of satellite data by compressing multispectral datasets into PC bands, it also segregates noise components by suppressing irradiance effects, eliminating data redundancy, and calculating a new coordinate system for it. Furthermore, it largely preserves the crucial information present in the images. PCA in image data involves three key steps: 1) determining variance from the data matrix; 2) finding eigenvalues and eigenvectors from the variance matrix; and 3) transforming the image data linearly using the eigenvector coefficients [127]. PCA is widely employed for lithological mapping by utilizing spectral bands from remote sensing sensors as this method consistently demonstrates a 90% effectiveness in geological discrimination and mineral exploration results as supported by numerous studies [113], [128], [129], [130]. The former [see Fig. 5(a)] was applied to distinguish and confirm the separation of felsic granitoid rocks from mafic ones in the study area. In contrast, the latter [see Fig. 5(b)] was employed to accurately identify the distribution of OPH rocks and to distinguish between various types of granite rocks in the study area, in addition to separating the NSS from the basement rock of the studied terrain.

4) Independent Component (IC) Analysis: ICA is a statistical and advanced computational method for extracting features by separating source signals from mixed ones, it can be utilized with multispectral or hyperspectral remote sensing data to reveal underlying factors in sets of random variables, or signals [131], [132]. This statistical technique operates on data through rotation in an n-dimensional space, where n represents the number of bands aiming to maximize the independence of the input data, as described by [133]. Furthermore, the resulting ICs are not just uncorrelated, akin to PCA, but they are also independent and possess detailed features, even when they represent a limited portion of image pixels [123]. The ICA can serve various purposes, including extracting image characteristics, reducing noise, separating features, identifying end-members, pinpointing targets and anomalies, as well as performing classification and mapping tasks [111], [134], [135]. In the current study, ICA 4-1-3 in RGB and ICA 1-4-5 in RGB as shown in Fig. 5(c) and (d) delivered superior results.

C. Machine Learning

1) Data Preparation and Feature Extraction: The current study dedicated significant time and effort to developing reference geological maps, aiming for a more precise identification of the exposed rock units in the study region. This involved amalgamating information from over five previous geological maps, employing various image processing techniques (FCC, DS, PCA, and ICA), conducting field investigations, and interpreting images. The integration of these various approaches not only facilitates accurate lithological discrimination but also enhances feature extraction, enabling a more effective separation of the training and testing data required for generalizing and evaluating processes. OPHs, island AMVs, OGs, MGs, SGs, dykes and shear zones (DY-SHZs), NSS, and wadi deposits (WDs) were the eight classes identified (see Table II). The latter describes the training and test data for these classes. Previous studies consistently advise the allocation of a range between 70% and 80% for training samples and 30%–20% for testing samples [43]. Accordingly, training samples specific to each rock unit were chosen, falling within the percentage range of 70%–80% (as shown in Table II). For better allocation of the classified targets, Shebl et al. [136] recommended increasing the number of informative inputs for the utilized algorithms.

Our current research applied several trials to resolve the conflicts among the previous lithological maps of the studied terrain. However, two main data inputs were selected in the current research for feeding SVM. The main input datasets (used to train SVM) are FCC 12-6-2 in RGB, respectively, and the fused (using stacked-vector method) FCC 12-6-2 + PCA 1-2-3 + ICA 1-4-5. The latter combination was selected based on our visual interpretation and analysis of all the resultant images. The data fusion was performed by creating comprehensive pixel vectors by combining different spectral information through various informative data points.

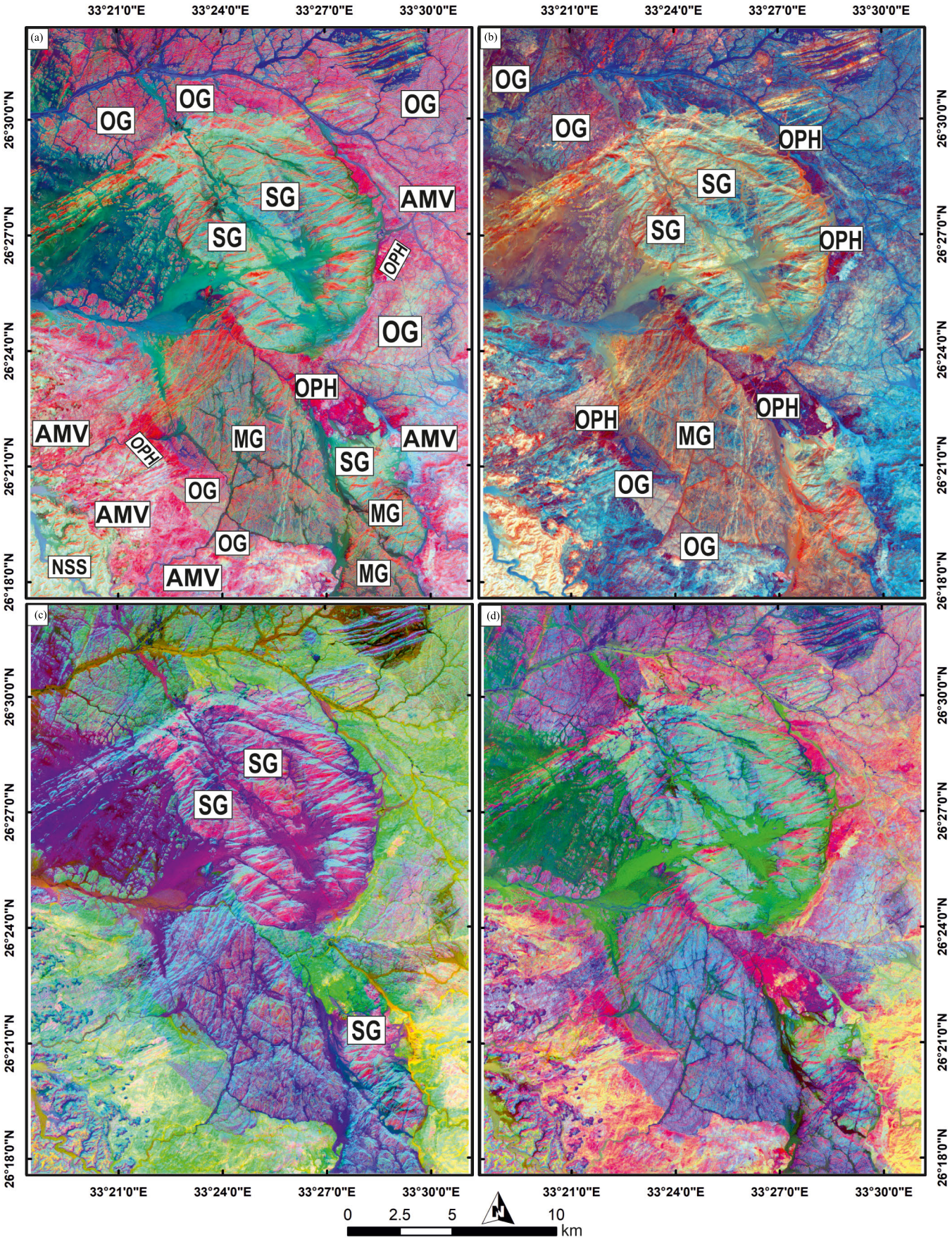

Fig. 5. Lithological characterization utilizing Sentinel-2 transformation combinations of (a) PCA 1-2-3, (b) PCA 4-2-3, (c) ICA 4-1-3, and (d) ICA 1-4-5 in RGB channels.

TABLE II
TRAINING AND TESTING DATA USED FOR THE LITHOLOGICAL ALLOCATION

Classes	Training Data		Testing data	
	Pixels	Percent	Pixels	Percent
Ophiolites (OPH)/Gabbros	235	0.70	97	0.29
Arc Metavolcanics (AMVs)	741	0.75	238	0.24
Older Granitoids (OG)	663	0.77	198	0.22
Monzogranites (MG)	693	0.72	261	0.27
Syenogranites (SG)	760	0.78	212	0.21
Dykes and shear zones (DY/SHZ)	793	0.76	249	0.23
Nubian sandstone (NSS)	620	0.76	190	0.23
Wadi deposits (WD)	703	0.77	206	0.22

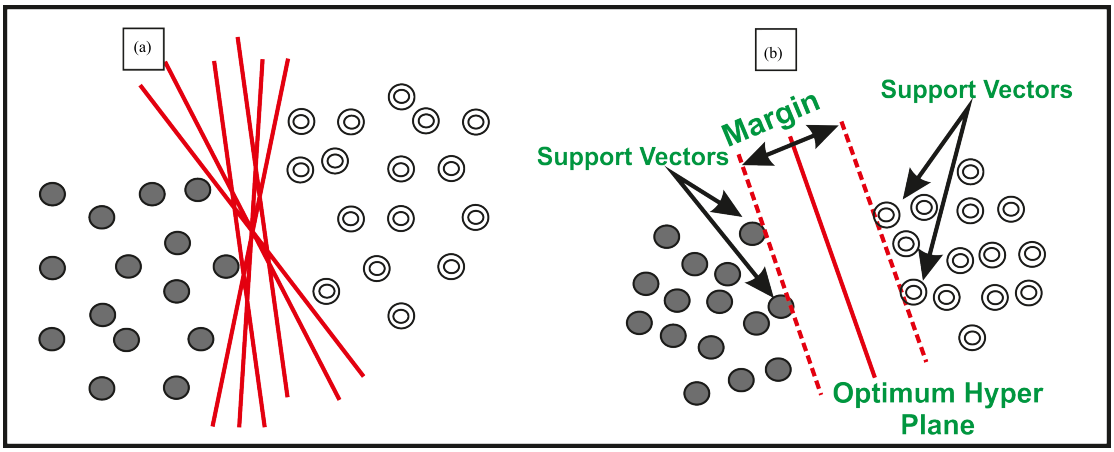

Fig. 6. (a) Hyperplanes for linearly separable data and (b) optimum hyperplane support vectors.

The information is merged using the extended-vector method as introduced by [137] and further utilized by [18]. The current study has opted to employ SVM as a machine learning tool, primarily because of SVM's recognized potential and precision in the classification of various rock types [138], [139], [140].

2) Support Vector Machine: SVM algorithms represent a category of supervised machine learning models rooted in statistical learning theory, often considered as heuristic [141]. In the context of classification, SVM aims to identify an optimal hyperplane that effectively segregates two classes as indicated in Fig. 6. This optimal hyperplane is ascertained by utilizing training datasets and subsequently validated through the assessment of its generalization capacity on test datasets. In the case of classifying n-dimensional datasets, SVMs generate a (n–1)-dimensional hyperplane. A singular hyperplane that maximizes the margin between these classes is known as the optimum hyperplane as illustrated in Fig. 6. The data points that exert influence over the margin's width are referred to as support vectors [142], [143]. SVM was selected as an MLA in the current research due to its proven effectiveness in several remote sensing applications [144], [145], [146], [147] including lithological mapping [25], [41], [42], [43], [138], [139], [140]. In our study, the SVM classifier is trained on Sentinel-2 data that is processed by FCC 12-6-2 in RGB channels alone and FCC 12-6-2 + PCA 1-2-3 + ICA 1-4-5 data.

IV. RESULTS AND DISCUSSION

Based on the generalization findings presented in (see Table III) and further elucidated in Fig. 7(a) marked superiority of the thematic maps emerges when the classifier is fed by the more informative datasets (FCC 12-6-2 + P-C-A 1-2-3 + ICA 1-4-5) rather than FCC alone as evidenced by the data presented in Fig. 7(a) and (b). This substantial enhancement can be primarily attributed to the enhanced characterization and separation of individual classes, resulting in a more precise localization of the decision boundary within the multidimensional dataset. This improved characterization arises from the greater contribution of informative pixels within the (FCC 12-6-2 + PCA 1-2-3 + ICA 1-4-5) combination, as compared to the more limited features provided by FCC alone. This, in turn, empowers the classifier to resolve numerous issues inherent to the complex classes, leading to an overall accuracy (OA) increase of more than 15%. This achievement is particularly noteworthy considering that this substantial improvement is achieved without altering the training and testing datasets. It's worth noting that despite these improvements, some misclassifications remain. The latter can be justified, given the

TABLE III
CONFUSION MATRIX, PA, UA, OA, AND KAPPA COEFFICIENT (K) OF SVM CLASSIFICATION RESULTS

Using FCC 12-6-2	OPH-Gabbro	MVS	OG	MG	SG	NSS	Dykes	Wadi	Total	Prod. Acc.	User. Acc.
OPH/ Gabbro	70	0	0	0	0	0	1	0	71	72.16	98.59
AMVs	0	182	4	0	0	70	0	0	256	76.47	71.09
OG	0	8	101	29	12	5	12	1	168	51.01	60.12
MG	0	0	54	100	18	0	12	0	184	38.31	54.35
SG	0	0	2	0	170	0	17	8	197	80.19	86.29
DY-SHZ	21	0	30	129	12	14	206	0	412	82.73	50
NSS	0	48	6	2	0	101	1	0	158	53.16	63.92
WD	6	0	1	1	0	0	0	197	205	95.63	96.1
Total	97	238	198	261	212	190	249	206	1651	OA= 68.26%	KC= 0.63
Using FCC 12-6-2, PCA 1-2-3 and ICA 1-4-5											
OPH / Gabbro	88	0	0	0	0	0	0	0	88	90.72	100
AMVs	0	223	4	2	0	11	0	0	240	93.7	92.92
OG	0	14	115	29	5	0	2	0	165	58.08	69.7
MG)	0	0	72	135	9	0	0	0	216	51.72	62.5
SG	0	0	2	5	197	0	8	0	212	92.92	92.92
DY-SHZ	5	0	4	86	1	4	239	0	339	95.98	70.5
NSS	0	1	1	2	0	175	0	0	179	92.11	97.77
WD	4	0	0	2	0	0	0	206	212	100	97.17

complexity of the geological setting of the terrain, which has exhausted many previous studies [47], [57], [58], [62], [63], [64], [65]. This complexity served as a primary motivation for undertaking this research and applying MLAs for the first time in the study area.

Generally, misclassifications are often attributed to the closeness in the spectral characteristics of the studied rock units, several deformation events, dykes, fractures, hydrothermal alterations (silicification, sericitization, hematization, greisenization, kaolinization, and fluoritization) [81], [87], [106], [148], and weathering products that may obscure the original features for each rock type causing bewilderment for the classifier.

For instance, the study area contains three types of granitoid rocks, younger granites (YGs) that are represented by SGs, MGs, and OGs that are typified by granodiorite. These granitic rocks have common mineralogical constituents such as quartz, plagioclase, k-feldspar, mica (biotite and muscovite), and amphiboles (hornblende), resulting in similarity in their appearance. In the study area and with more details, SGs consist of 59% quartz and 16% plagioclase as felsic minerals, with 1% biotite and 3% muscovite as mafic minerals [82]. MGs contain 51% quartz and 39% plagioclase as felsic minerals, along with 6% biotite as mafic minerals [82]. OGs are mainly composed of 39% quartz, 39% plagioclase, 6%–12% K-feldspar as felsic minerals, 13% biotite, and 1% hornblende as mafic minerals [81]. There is a degree of similarity in the mineral composition among the prominent granite types found in the study area and this is reflected by occasional misclassifications by the SVM algorithm.

These similar characteristics are more conspicuous in the case of the first generalization process (utilizing FCC 12-6-2 in RGB only) by the existence of several errors among the three classes as depicted in Fig. 8. For instance, MG has been misclassified as SGs and older granite resulting in a very low producer accuracy (PA) as shown in Fig. 7(a) and Table III. Similarly, older granite has been sometimes misclassified as SGs or MGs. These misclassifications are reflected in Fig. 7(a), where the two lowest values of the producer accuracies are related to MGs and older granite, respectively.

Furthermore, the wide range of mineralogical compositions of the AMVs exposed in the study area sometimes makes bafflement for the algorithm especially noticed with NSS. These disordered allocations are well-noticed in the thematic map provided only using FCC 12-6-2 in RGB due to the lack of further details discriminating between MVs and NSS. Although acidic metavolcanics (metadacites) are comparatively rare. Intermediate (metaandesites), and basic rocks (metadolerite, metabasalt, and amphibolite) also can be found and largely distributed. These basic to intermediate

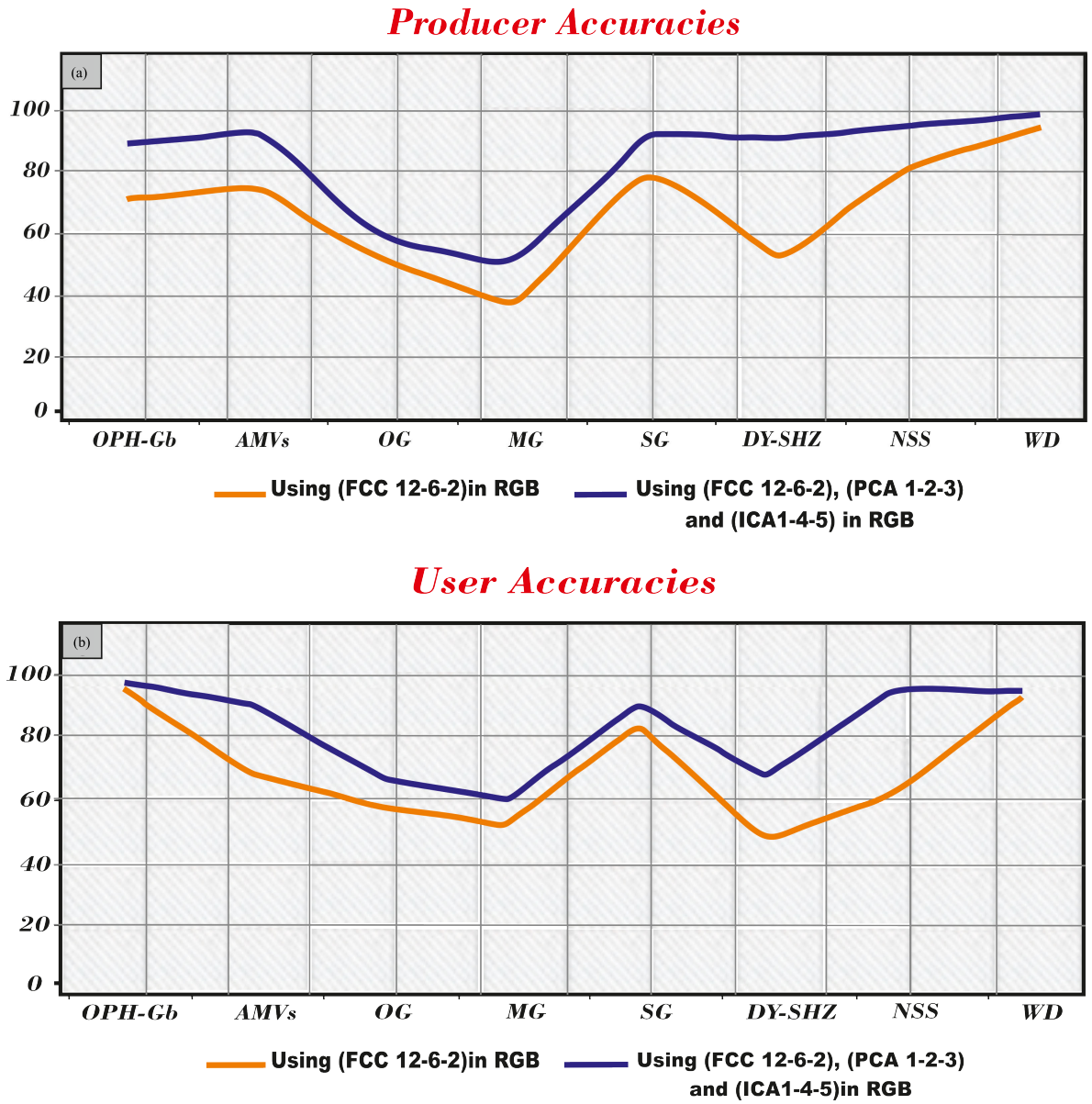

Fig. 7. (a) PA and (b) user accuracy (UA) for each class showing how well the classification is enhanced by adding PCA 1-2-3 and ICA 1-4-5 to FCC 12-6-2 in RGB channels.

metavolcanics are rich in hornblende and relics of pyroxene interpreting the higher iron content leading to these misclassifications with ferruginous NSS. Since the metavolcanics may contain a significant amount of iron (mainly intermediate to basic) represented by the dominance of hornblende and biotite, it could be the main reason for perplexing the SVM with NSS often characterized as ferruginous.

Our interpretation regarding these confusions among MVs and NSS has been evidenced by reports from previous studies that highlighted the heterogeneity within AMVs. Kassas and Bakhit [58] reported that the AMVs are extensively scattered throughout the entire surveyed region, representing a significant collection of metamorphic rocks with a volcanic igneous origin. These rocks can also occur as sizable xenoliths within the subsequent plutonic igneous formations like granodiorites and granites. These rocks typically exhibit a fine to medium-grain texture, appearing as solid and dense formations, and are characterized by dark green to grayish-green or dark gray shades. In some instances, near granite intrusions, you may observe hints of yellowish cream and light grayish hues in the outcrops. YG plutons like G El-Erediya intruded into these rocks, causing widespread faulting and fractures. Numerous quartz veins and a few newer, basic, acidic dykes are frequently responsible for injecting them. The diversity and heterogeneity within metavolcanics contribute to the misclassification of this rock unit, particularly when the algorithm is trained solely on a limited 12-6-2 in the RGB dataset.

OPHs also have a PA of around 72% (see Table III). This decrease is attributed to the intravariability within the class. This is thoroughly substantiated by several studies stating that OPHs in the studied terrain consist mainly of serpentinites, metagabbros, amphibolites, and ophiolitic mélange (metasediments) [47], [67] which are poorly discriminated and have a very small extent to be separated as individual classes. Despite

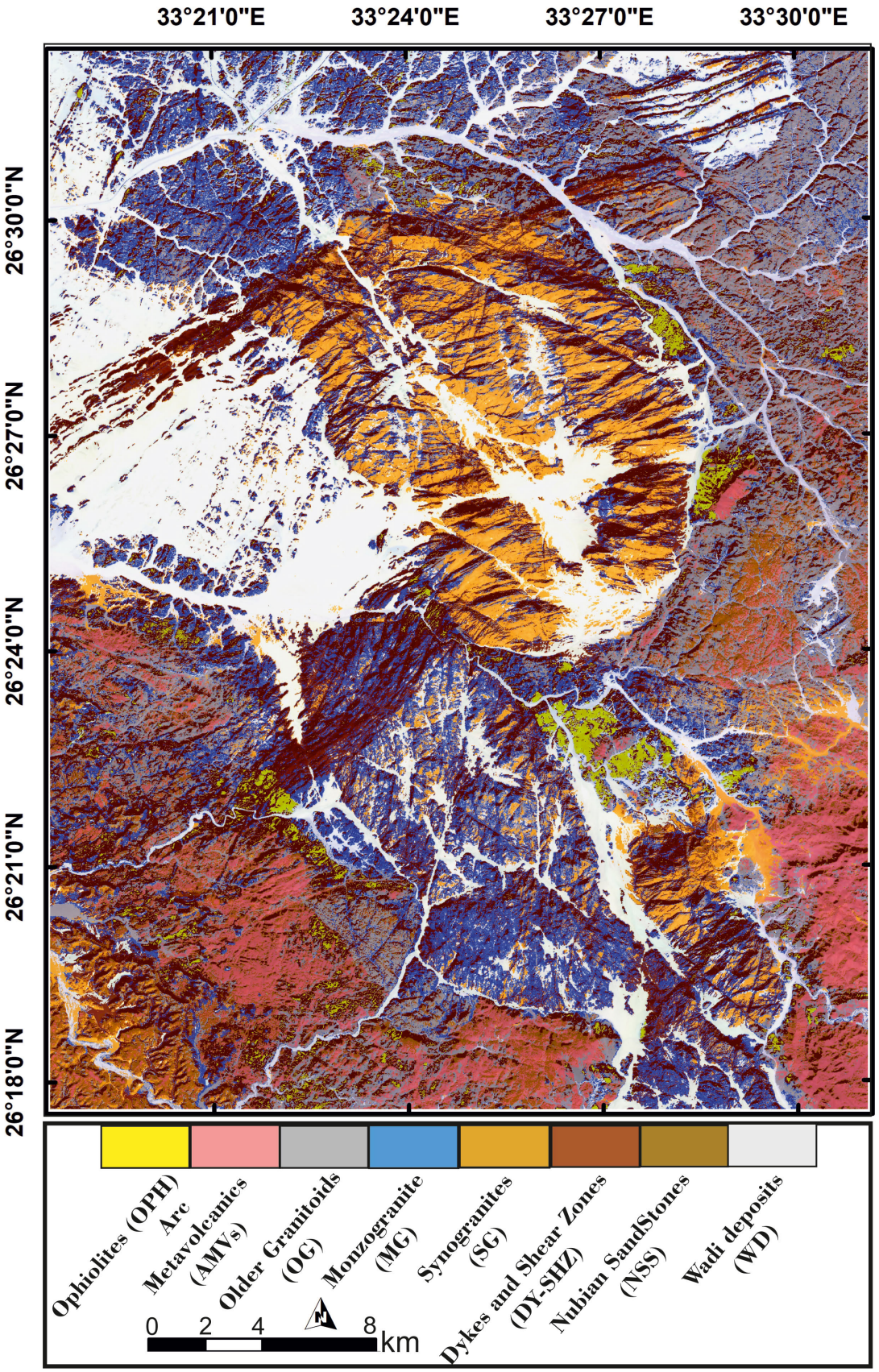

Fig. 8. Lithological map of El-Missikat and El-Erediya areas using SVM classification based on Sentinel-2 FCC 12-6-2 in RGB channels.

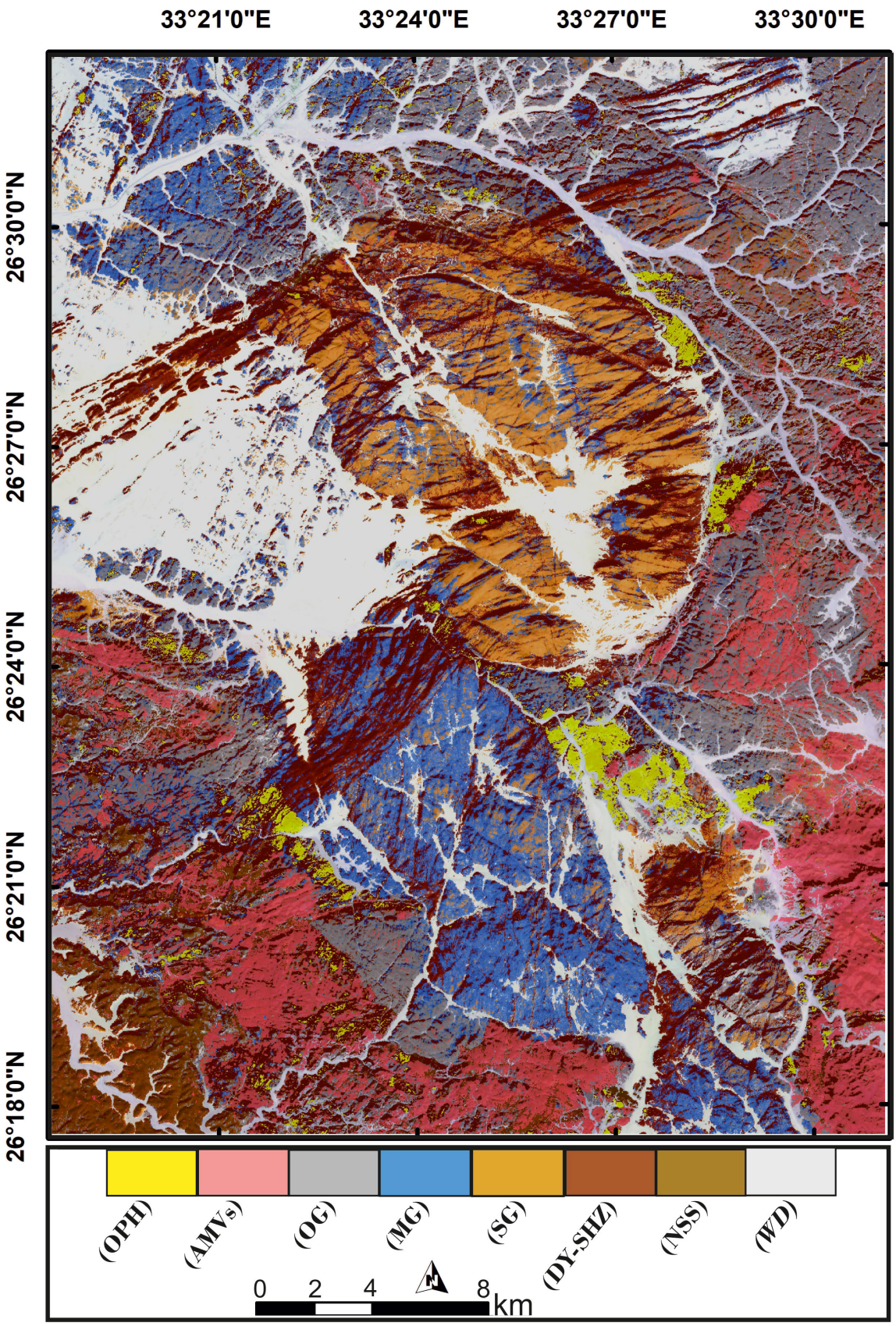

Fig. 9. Lithological map of El-Missikat and El-Erediya areas using SVM classification based on FCCs 12-6-2, PCA 1-2-3, and ICA 1-4-5 combinationsin RGB channels.

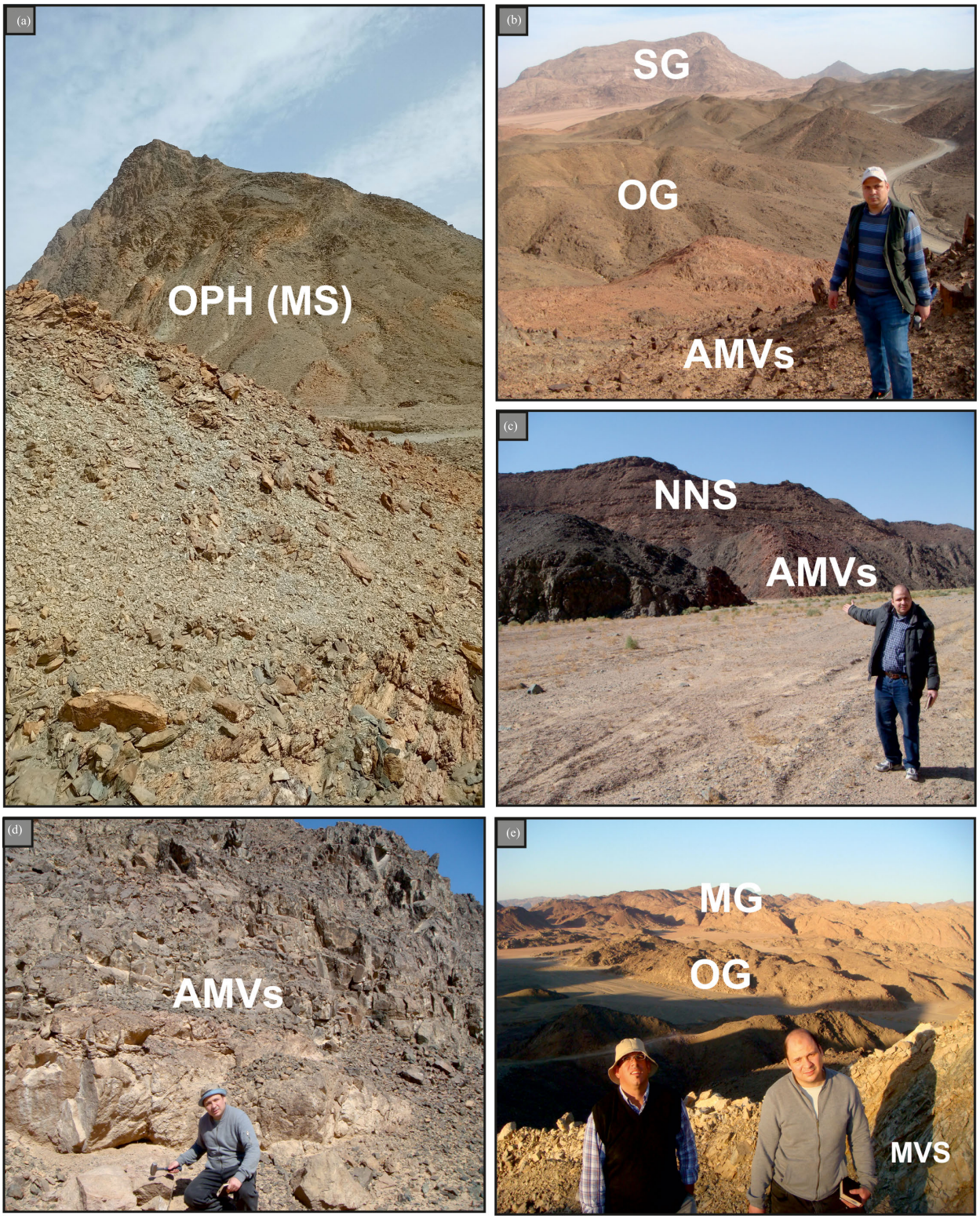

Fig. 10. Field photographs showing the mapped rock units of (a) ophiolitic metasediments in the eastern part of G. El-Erediya, (b) AMVs, older granites, and SGs that are located in the eastern area of G. El-Missikat and G. Ria El-Garra and northern G. El-Erediya, (c) general view of basic metavolcanics (basaltic andesite) that is located in the NE part of the area, (d) felsic metavolcanics that is situated in the western part of the G. El-Erediya and G. El-Maghrabiya, and (e) metavolcanics, older granites, and MGs in the western part of G. El-Maghrabiya. Symbols: OPH (MS) = ophiolite metasediments, AMVs = arc metavolcanics, OG = older granites, MG = monzogranites, NSS = Nubian sandstones, SG = syenogranites, and DY = dyke.

all of these differences, our classifier was able to accurately identify all the ophiolitic components within the study area compared to previous studies that mapped it with exhaustive efforts and time through field mapping.

To better tackle these misclassification problems, minimize error pixels in the classification of targets derived from basic input data, and address the discrepancies highlighted in prior studies, we employed FCC 12-6-2 + PCA 1-2-3 + ICA 1-4-5, as input for SVM. These composites were intentionally selected after comparing and visually interpreting more than 30 composites for the studied terrain. In addition, these composites include highly informative bands of the whole implemented Sentinel 2 bands. A distinct classification with sharper delineation of the complicated classes was evident both visually as indicated in Fig. 9 and statistically in Table III.

Visually, an understandable generalization and unambiguous allocation of MG as an elliptical block can be seen in Fig. 9 compared to the previous erroneous block filled with different types of pixels representing various classes in Fig. 8. Furthermore, in the southwestern corner of the study area, a lucid representation of NSS is presented in Fig. 9, compared to that shown in Fig. 8 with a lot of yellow error pixels representing SGs. The upgrading of the allocation is also manifested by comparing the AMVs, older granites, and OPHs all over the study area, where their flawed representations presented in Fig. 8 appear to be more coherent, corrected, and a bit sharp in Fig. 9.

All of these advancements are also undisputedly clear by comparing the statistical findings for each class. For instance, Table III and Fig. 7 show that comprehensive enhancements for all the classes are evident with different percentages. This statistical enhancement is better echoed by comparing the final OA and kappa coefficients for the two generalization processes. An apparent augmentation (by 15.2%) of the OA from 68.26% to 83.46% and for kappa coefficient (from 0.63 to 0.80) boosting was also noticed.

V. Field Verification of Generated Lithological Map

A comprehensive field reconnaissance plays a fundamental role in confirming the geological mapping that was obtained through the integration of remote sensing data and MLAs. The updated lithological map derived from Sentinel-2 data with SVM was field-validated through intensive field investigations as illustrated in Figs. 10–12 and the petrographic study in Fig. 13. The locations of the field photographs are dropped over Fig. 14 for more clarification. Several field stations (based mainly on accessibility) were visited and studied for the verification of all mapped lithological units and mineralized shear zones within the studied area as shown in Fig. 14. Our field investigations revealed a robust alignment with the updated classified map, indicating that the used method is effective for precise lithological mapping. The main finding of the current research is highlighting the higher capability of collaborative usage of the informative combinations (FCC12-6-2 + PCA1-2-3 + ICA1-4-5) of Sentinel 2 data and SVM for accurate lithological discrimination and better delineation of mineralized shear zones.

Our comprehensive field verification covered nearly all the lithological targets exposed within the study area, as indicated by our updated lithological map. Ophiolitic rocks are prevalent in the southern and eastern border of G. El-Missikat and G. Ria El-Garra, as well as in the eastern and northern regions of G. El-Eredia. Our investigations have confirmed the widespread distribution of ophiolitic rocks in eastern and western sections of G. El-Maghrabiya, as depicted in locations over Fig. 14. Addressing the distribution of these rocks within the study area stands out as a pivotal output in our research, given that previous geological mapping often grappled with inconsistencies [47], [58], [62], [66], [67], [148]. Nevertheless, the precise classification facilitated by Sentinel-2 processed images and SVM has successfully resolved this challenge. Subsequently, during field investigations, we conclusively confirmed the presence of these rock units, which could be characterized mainly as ophiolitic mélange (metasediments) in this area as evidenced by the data presented in Fig. 10(a).

The presence of AMVs on the northeastern, southeastern, and southwestern boundaries of the study area is evident and consistent with our updated lithological map, as depicted in Fig. 14, and corroborated by our field geological surveys, further illustrated in Fig. 10(b)–(e). Our updated lithological map shows that the AMVs are occasionally cut by several dykes. This setting was confirmed by our field investigations. For instance, the basic metavolcanics that appear in the NE part of the area (basaltic andesite) are cut with felsic dyke, and the latter cause melting to the former ones as shown in Fig. 11(b). Thus, xenoliths from the older AMVs inside the younger dyke could be seen in Fig. 11(c). Felsic metavolcanics are also distributed in the SW corner of the area (Wadi Hamama metavolcanics), the latter exhibits some color transformations because of the hydrothermal alterations as illustrated in Fig. 10(d). They are characterized by columnar joints in several locations [see Fig. 11(d) and (e)].

OGs are broadly distributed in the study (e.g., NE, NW part, and in the western part of G. El-Maghrabiya and G. El-Eredia) as displayed in Fig. 14. Through our field reconnaissance, older granites have also been validated as shown in Fig. 10(b) and (e). MG units are represented mainly by G. El-Maghrabiya and the southern part of G. El-Eredia as displayed in Fig. 14. A field survey was undertaken, and these granitic rocks also have been justified as evidenced by the data presented in Figs. 10(e) and 12(a)–(c). SGs represented by G. El-Missikat, G. Ria El-Garra, G. El-Gidami, and the northern part of G. El-Eredia as shown in Fig. 14, have also been confirmed through field reconnaissance, as demonstrated in Figs. 10(b) and 12(d).

DY-SHZs that are considered significant mineralized zones within the study area are meticulously checked in our updated lithological map with field investigations and the known potential mineralized spots reported from previous studies. These zones are mainly revealed in the northern part of G. El-Missikat, along the contact between G. El-Missikat and G. El-Maghrabiya (Northern G. El-Maghrabiya) as well, in the southern part of G. El-Eredia as demonstrated in Fig. 14.

Our results accurately identified the shear zones and showed a marked consistency with the distributions of radioactive mineralizations (areas with white squares), indicated by many previous studies [56], [62], [66], [67], [80], [81], [88], [148], [149]. It should be emphasized that this accurate detection

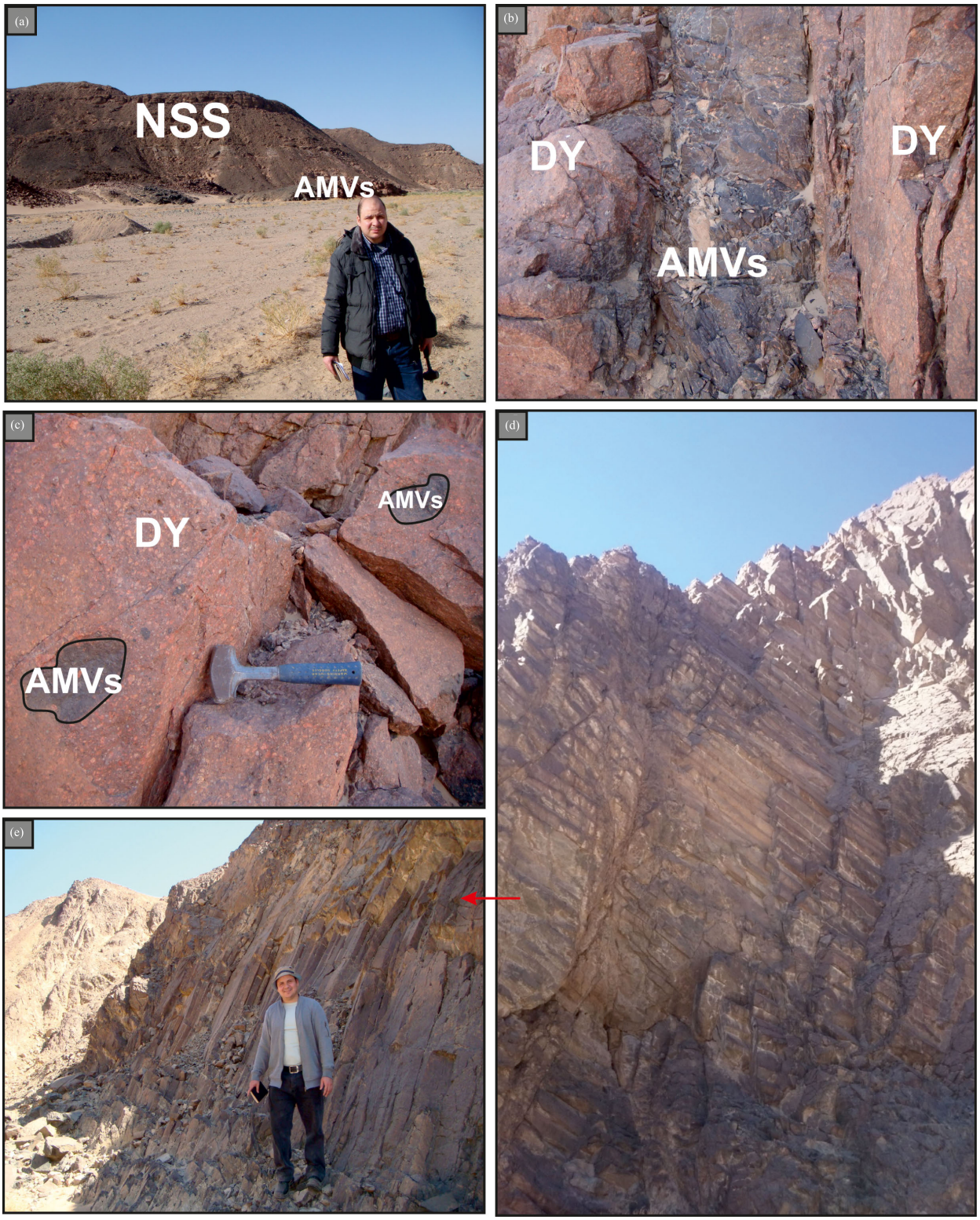

Fig. 11. Field photographs showing the mapped rock units of (a) general view to the metavolcanics (basaltic andesite) and NSSs is revealed in the back of the area, (b) felsic dyke that cut the basic metavolcanics, (c) inclusions of basic metavolcanics within the felsic dykes, and (d) and (e) general and closer view to felsic metavolcanics exhibiting columnar joints. Symbols: AMVs = metavolcanics, DY = dyke, and NSS = Nubian sandstones.

of these mineralized shear zones was carried out depending mainly on accurate lithological separation emphasizing the role of the enhanced lithological mapping in saving time, costs, and efforts for detecting mineralized terrains.

Our field check highlighted that NSS is revealed in the SW corner of the area of study as illustrated in Fig. 14 and shows great consistency with our updated lithological map as shown in Figs. 11(a) and 12(e). WDs are distributed all over the area

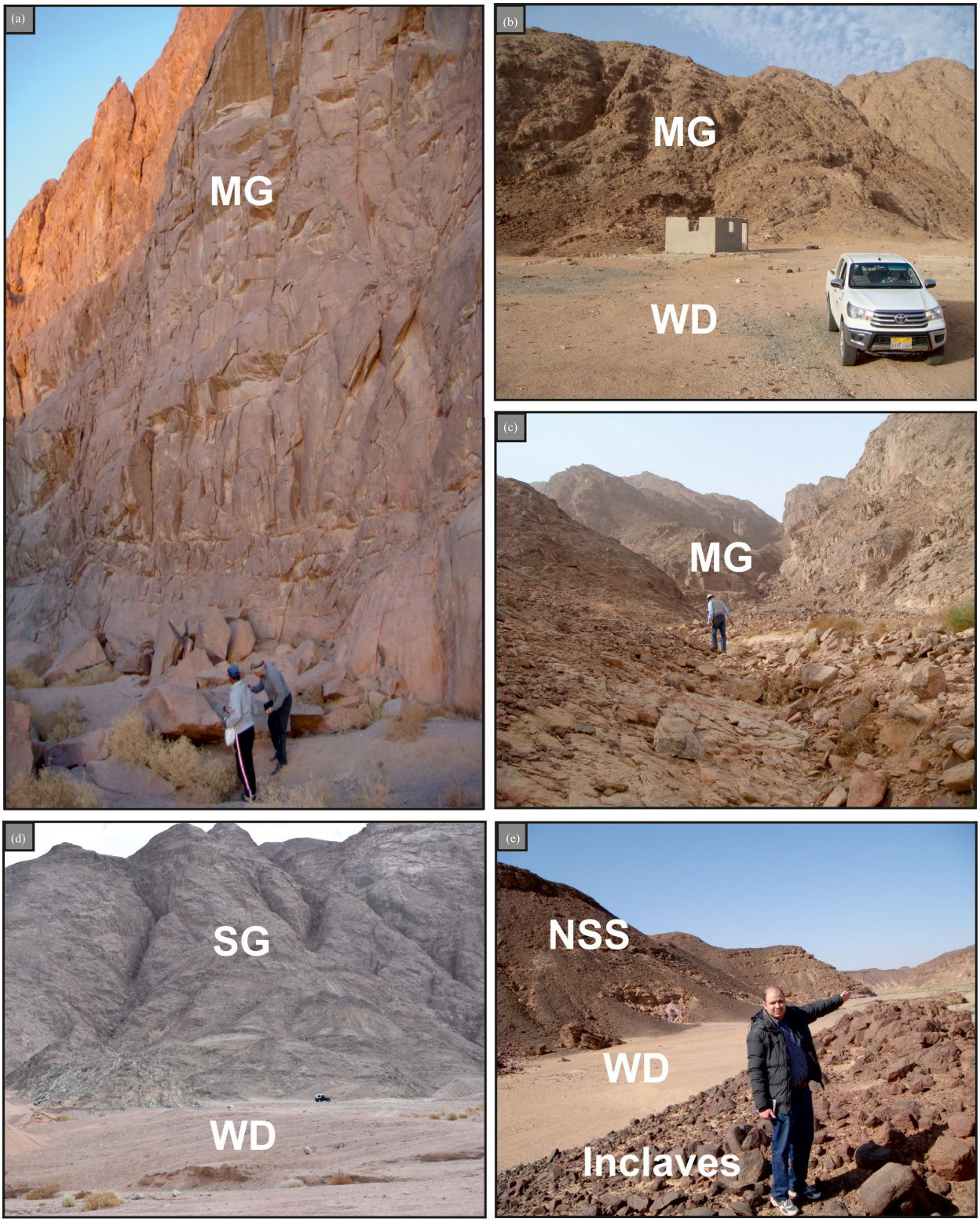

Fig. 12. Field photographs showing the mapped rock units of (a) MGs at the western part of G. El-Maghrabiya, (b) MGs at the western area of G. El-Eredіya, (c) MGs at the eastern part of G. El-Eredіya and G. El-Maghrabiya, (d) SGs at the northern western part of G. El-Missikat (opposite to El-Missikat mine) and (e) inclaves inside granitic porphery and pointing to the strike of the dyke and this photograph also show the contact between metavolcanics and NSSs. Symbols: MG = monzogranites, SG = syenogranites, DY = dyke, NSS = Nubian sandstones, and WD = Wadi deposits.

as displayed in Fig. 14 and are validated in several locations as depicted in Fig. 12(b), (d), and (e).

Overall, the rock units observed in the field locations closely match the predictions presented on our lithological map, a product of the integration of enhanced Sentinel-2 images and the SVM model. Notably, this approach effectively distinguished mineralized shear zones, offering the opportunity to focus expensive geophysical and geochemical analyses on

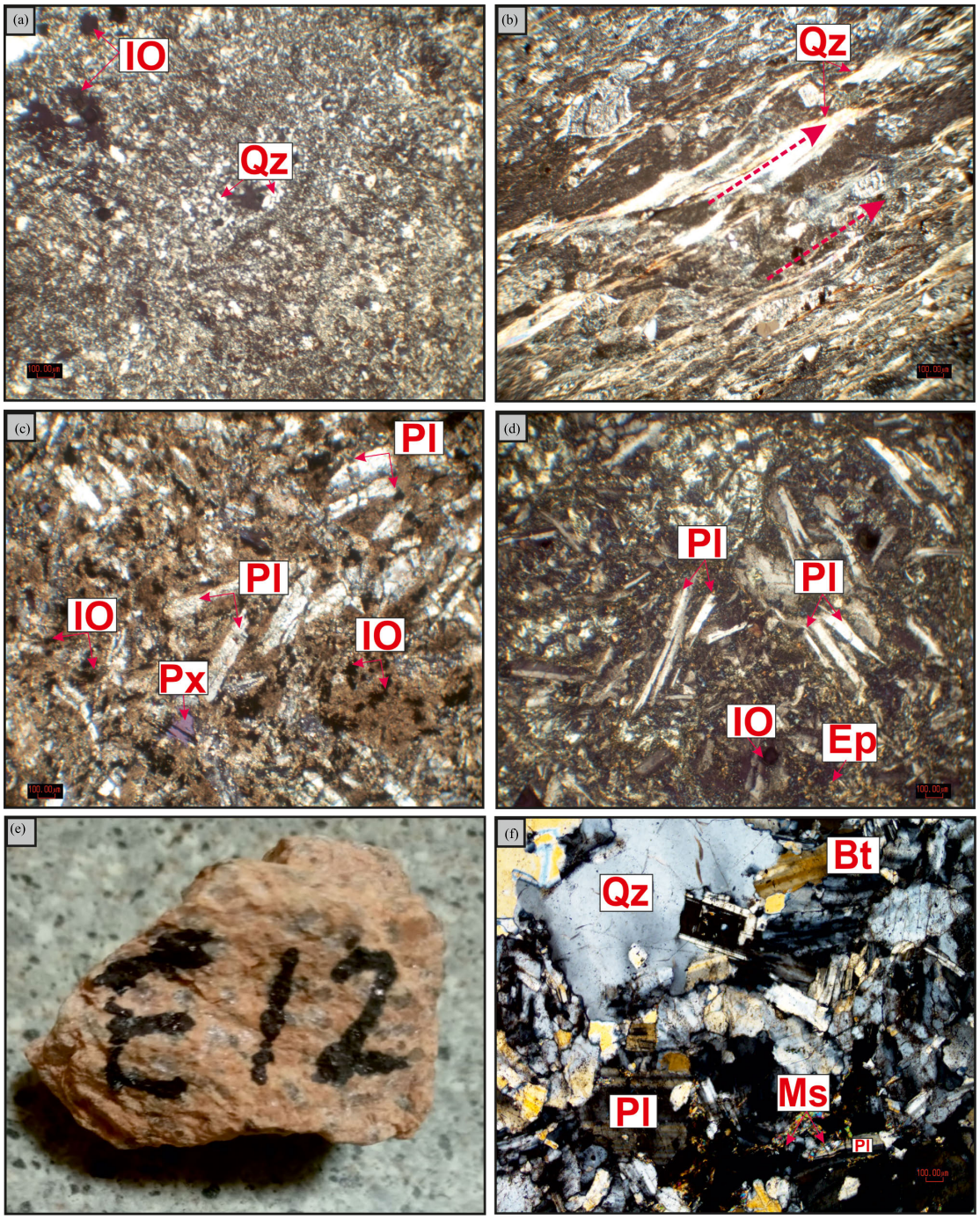

Fig. 13. Cross-polarized (XPL) photomicrographs showing, (a) fine ophiolitic metasediments, (b) coarse ophiolitic metasediment exhibiting dominant foliation, (c) and (d) basic metavolcanics (basaltic andesite), showing blasto-intergranular texture, (e) hand specimen of unaltered YG from El-Erediya pluton and it is located far away from the shear zones (SG), and (f) SG, showing hypidiomorphic texture. Symbols: Qz = quartz, Pl = plagioclase, IO = iron oxides, Bt = biotite, and Ms = muscovite. Hand specimens accompanied by thin sections of altered granites bearing U-mineralization showing.

these areas. This underscores the pivotal role of integrating MLAs with remote sensing data in applications of this nature. It is worth highlighting that a meticulous examination of all predicted shear zones on our final lithological map revealed a remarkable alignment with the well-documented mineralized zones within the study area as depicted in Fig. 14.

Petrographically, previous research [58], [81] has predominantly concentrated on granitic rocks, as noted and described in the geological context of our current study. As a result, our primary petrographic investigations were specifically tailored to examine ophiolitic metasediments and AMVs, also in addition to some granitic varieties, including unaltered and altered mineralized sheared granitoids. We selected these rock types due to their extensive distribution, covering a significant portion of the study area.

Ophiolitic metasediments exhibit fine to medium grain size texture and a color range from light gray to black. They consist primarily of quartz and feldspar crystals intensively

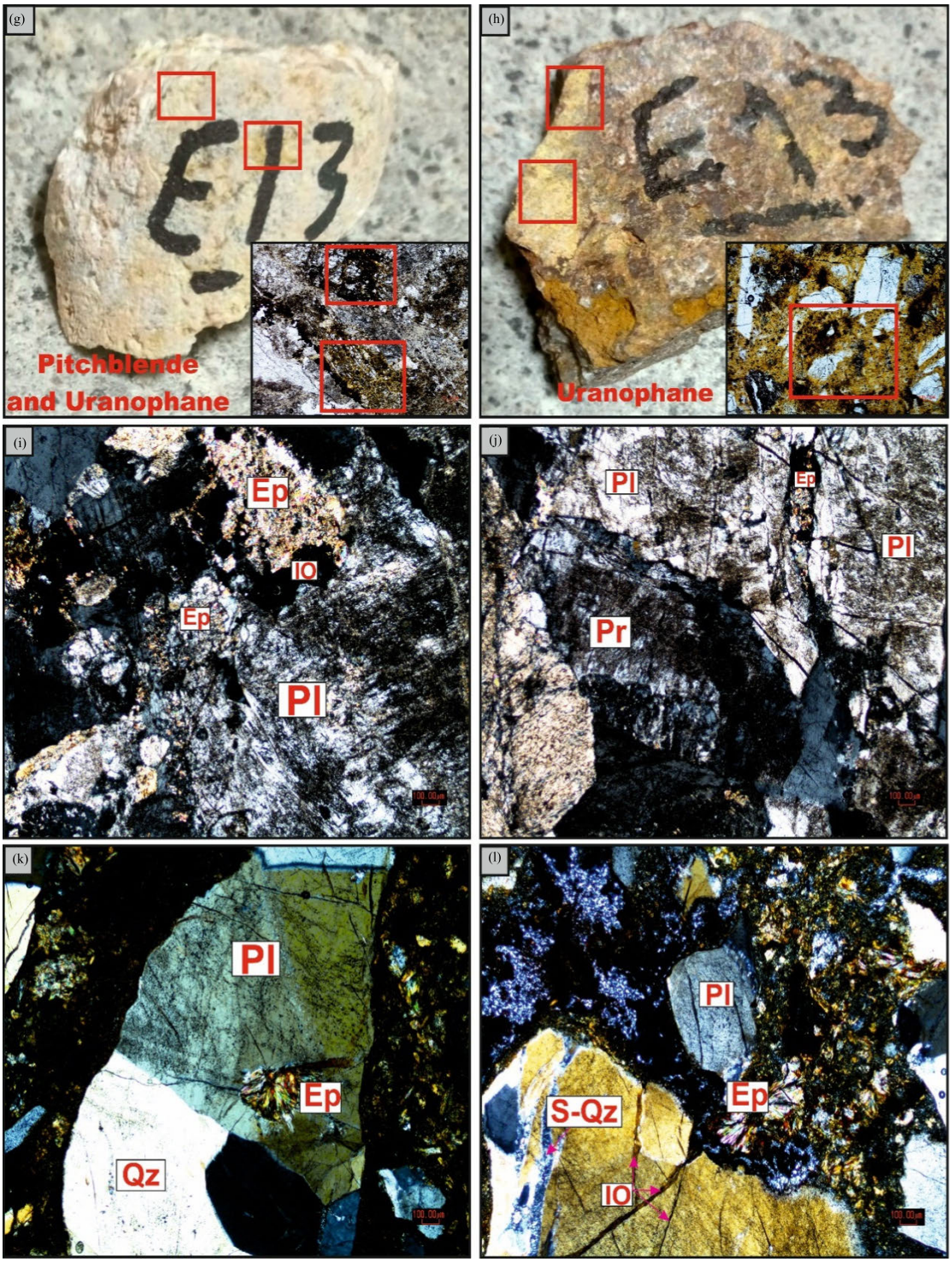

Fig. 13. *(Continued.)* Cross-polarized (XPL) photomicrographs showing, (g) primary and secondary U-minerals situated in the fractures and cracks in the shear zones, (h) U-mineral bearing granite (uranophane) from the shear zone that situated in El-Erediya pluton, XPL photomicrographs showing, (i) and (j) highly alteration of plagioclase to sericite and epidote, (k) fan shape pleochroic epidotes indicating to the high radioactivity, and (l) radioactive YG that contains iron oxides and secondary quartz veinlets showing the effect of hydrothermal solutions. Symbols: Ep = epidote, Pl = plagioclase, IO = iron oxides, Pr = perthite, Qz = quartz, and S-Qz = secondary.

altered to secondary clay minerals, as depicted in Fig. 13(a), and occasionally display foliations, as seen in Fig. 13(b). AMVs encompass a variety of types, with basic to intermediate metavolcanics, such as basaltic andesite, being the predominant types. These metavolcanics are composed of fine laths of plagioclase and actinolite as essential minerals, along with opaques mainly iron oxides, and sphene as accessory minerals. Fig. 13(c) illustrates the high alteration of plagioclase laths into epidote and sericite, and some crystals display simple lamellar twinning, as shown in Fig. 13(d). Actinolite forms after the original pyroxene and is found in the interstices between the plagioclase laths. A distinct

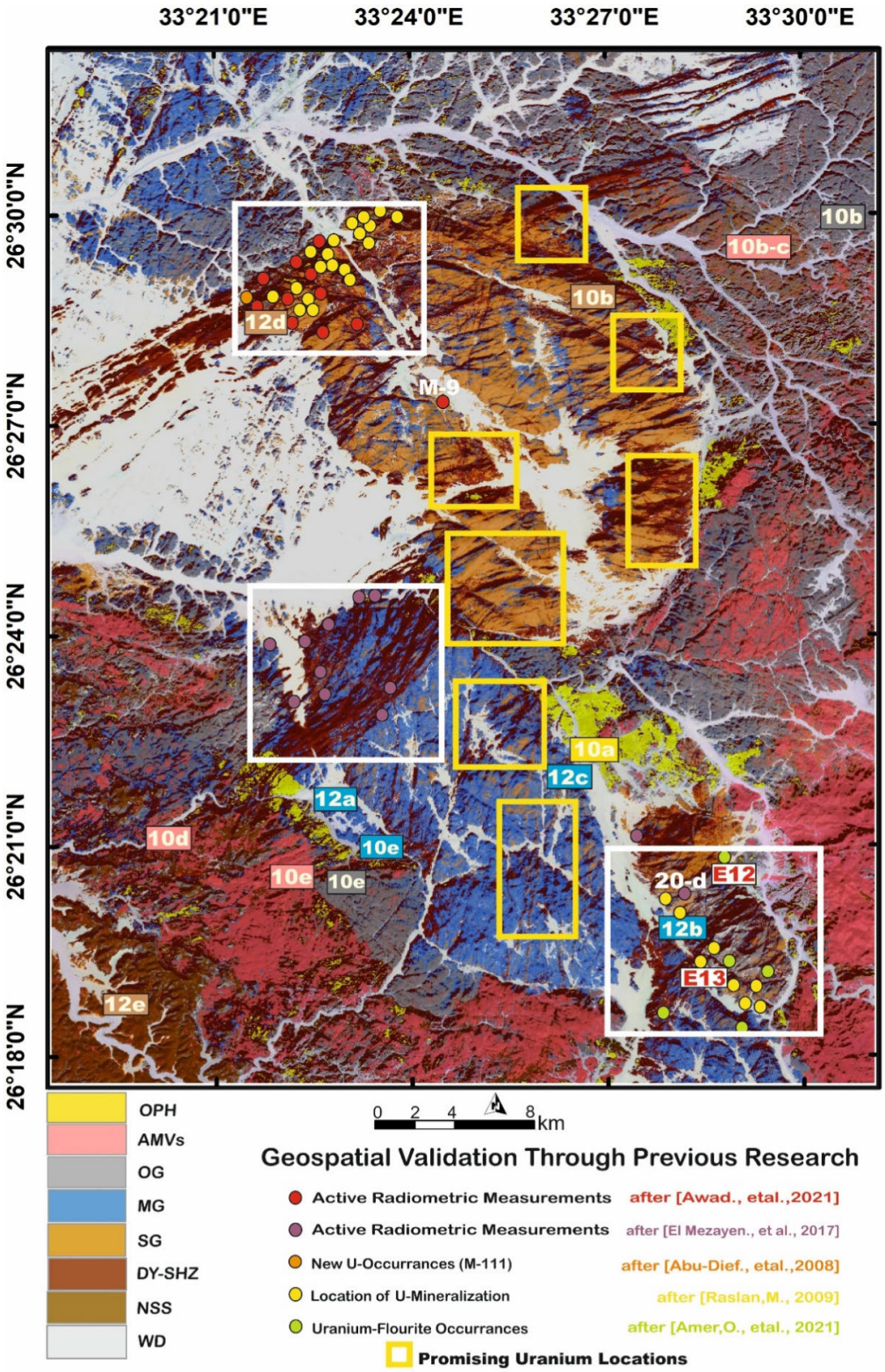

Fig. 14. Our updated lithological map illustrates a close alignment between the classified mineralized shear zones and previously identified mineralized areas from prior research. Field photograph locations (e.g., Fig. 10(a), (b), and so on) have been overlaid on the figure. The newly identified locations, delineated by yellow boxes, are considered promising sites for radioactive mineralization.

blasto-intergranular texture is well-defined, as seen in Fig. 13(c) and (d).

Unaltered (fresh) YGs are massive, coarse-grained, and buff to red, as shown in Fig. 13(e), and exhibit hypidiomorphic texture as displayed in Fig. 13(f). They consist mainly of potash feldspar (perthite), quartz, and plagioclase in combination with mafic components; mainly biotite and muscovite as seen in Fig. 13(f), together with zircon, apatite, and iron oxides as accessory minerals.

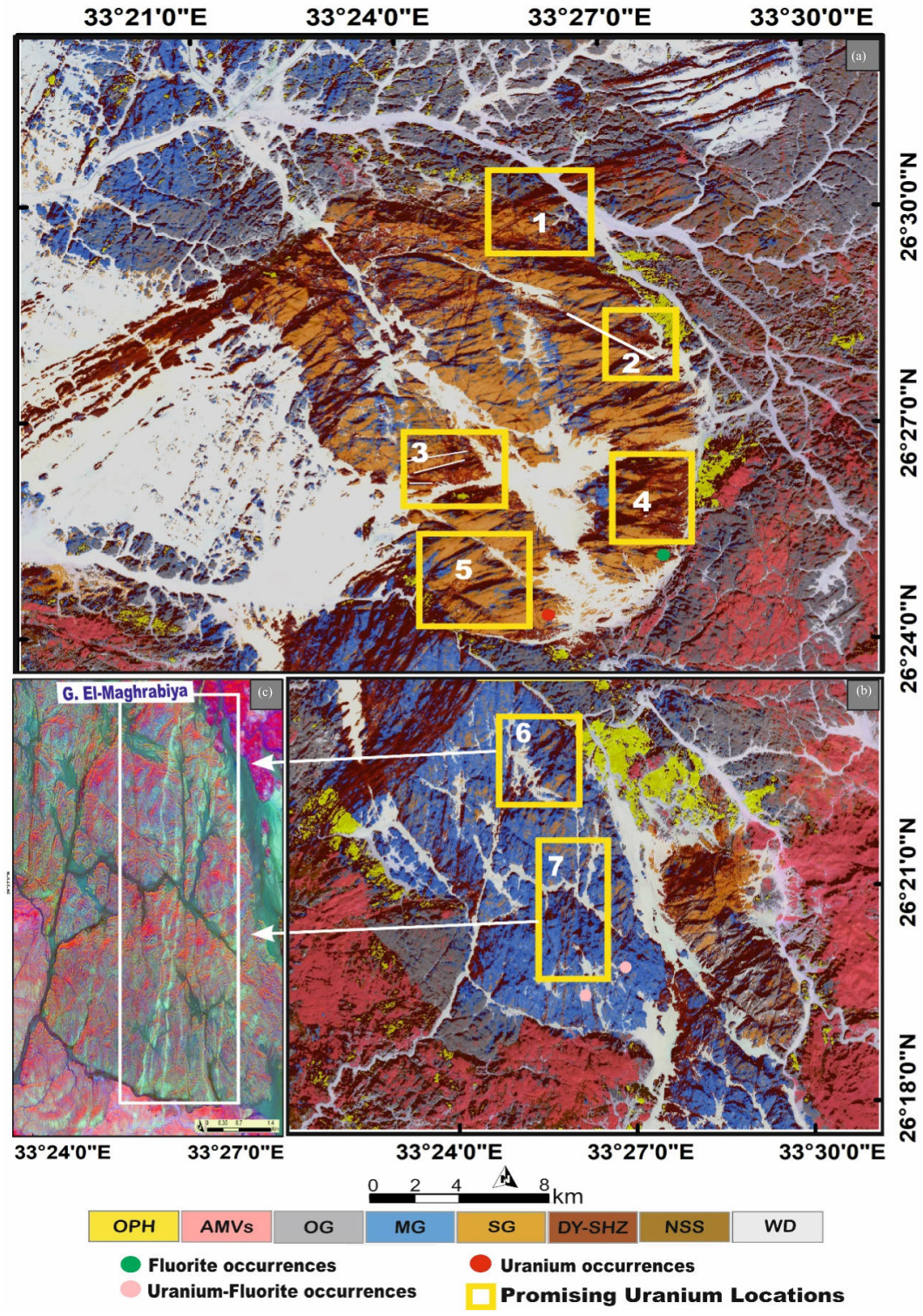

Fig. 15. Updated lithological map that shows newly identified areas where radioactive mineralization is likely to occur, (a) locations in G. El-Missikat, G. Ria El-Garra, and G. El-Gidami SGs, (b) locations in El-Maghrabiya MG and (c) detailed view of the new locations in El-Maghrabiya MG.

Hydrothermally altered granitoid rocks are impregnated with U-bearing mineralizations, like pitchblende, considered a primary uranium mineral, and uranophane, considered a secondary uranium mineral, as illustrated in Fig. 13(g). These minerals are discovered within the cracks and fractures present in the shear zones of El-Erediya pluton. Secondary uranium mineralization bearing granite (uranophane), that consistently manifests in a vibrant canary yellow hue and always resides in the shear zones as shown in Fig. 13(h). Fig. 13(i) and (j) shows the highly sheared granitic rock, signifying this through the highly altered plagioclase mineral to epidote and sericite. The fan shape of epidote minerals, this phenomenon holds significant importance, revealing both elevated radioactivity levels and the existence of radioactive mineralization, as vividly

depicted in Fig. 13(k). The discernible impact of hydrothermal solutions is showcased in Fig. 13(l), providing conclusive evidence for the presence of shear zones in the study area, abundant with numerous fractures, cracks, and fissures. These pathways enable the infiltration of solutions enriched with minerals, such as iron oxides and secondary quartz minerals, depositing them in the configuration of small veins within the radioactive granite. This aligns seamlessly with our findings, conclusively demonstrating the presence of shear zones within these areas.

The samples procured from the study area, specifically the hand samples derived from granitic rocks, demonstrate a noteworthy concordance with our acquired results. It is particularly noteworthy that the unaltered hand samples, strategically positioned at a significant distance from the shear zones as shown in Fig. 14 (sample E-12), consistently validate our remote sensing outcomes. Conversely, the altered samples, housing radioactive minerals, conspicuously cluster in proximity to and within the shear zones, as displayed in Fig. 14 (sample E-13). This enhances the accuracy of our results.

VI. Economic Implications of Precise Lithological Mapping

The precise identification of rock units and radioactive mineralized shear zones remains our core objective. Our findings demonstrate the significant achievement of integrating Sentinel 2 data with SVM. We have attained a favorable and satisfactory outcome that is largely harmonious with our field reconnaissance and the previously highlighted mineralization zones as displayed in Fig. 14.

Our final lithological map accurately highlighted the sheared zones and dykes within the study area. Geospatial overlay analysis of the known mineralized spots within the study area revealed that all the radiometric mineralized zones are located within the highlighted shear zones. This, in turn, confirms the reliability of the final geological map and narrows the areas to be further investigated for detailed mineral exploration and exploitation. In addition, the study highlights new potential areas across the entire study region (indicated by yellow squares) that could subsequently be targeted for radioactive mineralizations, as illustrated in Fig. 14.

Fig. 14 clarified that the results of the research were productive and confirmed the presence of radioactive mineralization within shear zones, consistent with findings from previous studies [66], [67], [81], [88], [148], [149]. The data points on the map illustrate the widespread occurrence of radioactive mineralization in these shear zones, which were effectively identified in the updated lithological map (white boxes). Furthermore, previous radiological measurements consistently showed high concentrations within these shear zones [62], [149].

Precise mapping to pinpoint areas rich in minerals is a critical starting point that leads to time and resource savings, especially in regions where radioactive minerals are prevalent. Our findings also led to the discovery of excavation sites that had not been previously mentioned in prior studies (indicated by yellow squares in Fig. 14) and (see Fig. 15). We are optimistic about conducting further research in these areas to extract new and supplementary minerals.

VII. Conclusion

The current research employed an SVM as an MLA to resolve complex lithological patterns and discrepancies among previous maps in the El-Missikat and El-Erediya regions, known for their significant radioactive-bearing mineralizations in Egypt. SVM provided substantial time and resource efficiencies compared to traditional field-based geological mapping, offering precise mineral location information. The study's key finding emphasizes the effectiveness of combining previous geological maps with spectral enhancement products generated from FCCs, PCA, and ICA in creating a reliable reference lithology map for feature extraction. Notably, augmenting false-color combinations with informative PCA and ICA outputs significantly improved OA by over 15%. For the first time, this research introduced an updated and objective lithological map of the study area, clearly delineating lithological boundaries and targeting mineralized zones, predominantly associated with shear zones. Field investigations and petrographic analysis validated our findings. We anticipate that this methodology will make a substantial contribution to the advancement of lithological mapping and mineral exploration in future research endeavors.

Declaration of Competing Interest

The authors declare that they have no known competing financial interests or personal relationships that could have appeared to influence the work reported in this article.

Data Availability

The datasets used and/or analyzed during the current study are available from the corresponding author upon reasonable request.

Acknowledgment

The authors thank to the European Space Agency (ESA) for providing the data. They thank to the University of Debrecen for the great support.

References

[1] J. Cardoso-Fernandes, A. C. Teodoro, A. Lima, M. Perrotta, and E. Roda-Robles, "Detecting lithium (Li) mineralizations from space: Current research and future perspectives," *Appl. Sci.*, vol. 10, no. 5, p. 1785, Mar. 2020, doi: 10.3390/app10051785.

[2] M. W. Mwaniki, M. S. Matthias, and G. Schellmann, "Application of remote sensing technologies to map the structural geology of central region of Kenya," *IEEE J. Sel. Topics Appl. Earth Observ. Remote Sens.*, vol. 8, no. 4, pp. 1855–1867, Apr. 2015.

[3] A. De, D. B. Upadhyaya, S. Thiyaku, and S. K. Tomer, "Use of multi-sensor satellite remote sensing data for flood and drought monitoring and mapping in India," in *Tracts in Civil Engineering*. Cham, Switzerland: Springer, 2022, pp. 27–41.

[4] M. A. Abdelkader, Y. Watanabe, A. Shebl, H. A. El-Dokouny, M. Dawoud, and Á. Csámer, "Effective delineation of rare metal-bearing granites from remote sensing data using machine learning methods: A case study from the umm naggat area, central Eastern desert, Egypt," *Ore Geol. Rev.*, vol. 150, Nov. 2022, Art. no. 105184, doi: 10.1016/j.oregeorev.2022.105184.

[5] Z. Wang, R. Zuo, and H. Liu, "Lithological mapping based on fully convolutional network and multi-source geological data," *Remote Sens.*, vol. 13, no. 23, p. 4860, Nov. 2021.

[6] A. Shebl, T. Kusky, and Á. Csámer, "Advanced land imager superiority in lithological classification utilizing machine learning algorithms," *Arabian J. Geosci.*, vol. 15, no. 9, p. 923, May 2022.

[7] A.-S. Høyer et al., "Development of a high-resolution 3D geological model for landfill leachate risk assessment," *Eng. Geol.*, vol. 249, pp. 45–59, Jan. 2019.

[8] A. D. Regmi, P. Cui, M. R. Dhital, and Q. Zou, "Rock fall hazard and risk assessment along araniko highway, central Nepal Himalaya," *Environ. Earth Sci.*, vol. 75, no. 14, pp. 1–20, Jul. 2016.

[9] G. Ielsch, M. Cuney, F. Buscail, F. Rossi, A. Leon, and M. E. Cushing, "Estimation and mapping of uranium content of geological units in France," *J. Environ. Radioactivity*, vol. 166, pp. 210–219, Jan. 2017.

[10] J. R. Harris and E. C. Grunsky, "Predictive lithological mapping of Canada's North using random forest classification applied to geophysical and geochemical data," *Comput. Geosci.*, vol. 80, pp. 9–25, Jul. 2015.

[11] A. Shebl, M. Abdellatif, S. O. Elkhateeb, and Á. Csámer, "Multisource data analysis for gold potentiality mapping of atalla area and its environs, central Eastern desert, Egypt," *Minerals*, vol. 11, no. 6, p. 641, Jun. 2021.

[12] B. L. Dickson and K. M. Scott, "Interpretation of aerial gamma-ray surveys-adding the geochemical factors," *AGSO J. Aust. Geol. Geophys.*, vol. 17, no. 2, pp. 187–200, 1997.

[13] G. Cheng et al., "Quantitative remote sensing of metallic elements for the qishitan gold polymetallic mining area, NW China," *Remote Sens.*, vol. 13, no. 13, p. 2519, Jun. 2021.

[14] L. Yu, A. Porwal, E.-J. Holden, and M. C. Dentith, "Towards automatic lithological classification from remote sensing data using support vector machines," *Comput. Geosci.*, vol. 45, pp. 229–239, Aug. 2012.

[15] M. A. El-Wahed, S. Kamh, M. Ashmawy, and A. Shebl, "Transpressive structures in the ghadir shear belt, Eastern desert, Egypt: Evidence for partitioning of oblique convergence in the Arabian-Nubian shield during gondwana agglutination," *Acta Geologica Sinica English*, vol. 93, no. 6, pp. 1614–1646, Dec. 2019.

[16] M. Z. Khedr et al., "Remote sensing and geochemical investigations of sulfide-bearing metavolcanic and gabbroic rocks (Egypt): Constraints on host-rock petrogenesis and sulfide genesis," *Gondwana Res.*, vol. 119, pp. 282–312, Jul. 2023.

[17] S. M. A. Khashaba, N. H. El-Shibiny, S. M. Hassan, E. Takazawa, and M. Z. Khedr, "Application of remote sensing data integration in detecting mineralized granitic zones: A case study of the gabal Al-Ijlah Al-Hamra, central Eastern desert, Egypt," *J. Afr. Earth Sci.*, vol. 200, Apr. 2023, Art. no. 104855.

[18] A. Shebl and Á. Csámer, "Stacked vector multi-source lithologic classification utilizing machine learning algorithms: Data potentiality and dimensionality monitoring," *Remote Sens. Appl. Soc. Environ.*, vol. 24, Nov. 2021, Art. no. 100643.

[19] M. Z. Khedr et al., "Remote sensing techniques and geochemical constraints on the formation of the wadi el-hima mineralized granites, Egypt: New insights into the genesis and accumulation of garnets," *Int. J. Earth Sci.*, vol. 111, no. 7, pp. 2409–2443, Oct. 2022.

[20] M. Badawi, M. Abdelatif, A. Shebl, F. Makroum, A. Shalaby, and N. Németh, "Mapping structurally controlled alterations sparked by hydrothermal activity in the Fatira–Abu zawal area, Eastern desert, Egypt," *Acta Geologica Sinica English*, vol. 97, no. 2, pp. 662–680, Apr. 2023.

[21] S. Gad and T. Kusky, "Lithological mapping in the Eastern desert of Egypt, the barramiya area, using Landsat thematic mapper (TM)," *J. Afr. Earth Sci.*, vol. 44, no. 2, pp. 196–202, Feb. 2006.

[22] S. Rajendran, S. Nasir, T. M. Kusky, and S. al-Khirbash, "Remote sensing based approach for mapping of CO_2 sequestered regions in samail ophiolite massifs of the Sultanate of Oman," *Earth-Sci. Rev.*, vol. 135, pp. 122–140, Aug. 2014.

[23] A. Emam, B. Zoheir, and P. Johnson, "ASTER-based mapping of ophiolitic rocks: Examples from the Allaqi–Heiani suture, SE Egypt," *Int. Geol. Rev.*, vol. 58, no. 5, pp. 525–539, Apr. 2016.

[24] A. Shebl and A. Csamer, "Lithological, structural and hydrothermal alteration mapping utilizing remote sensing datasets: A case study around Um Salim area, Egypt," in *Proc. IOP Conf. Ser. Earth Environ. Sci.*, 2021, p. 12032.

[25] A. Shebl et al., "Impact of DEMs for improvement sentinel 2 lithological mapping utilizing support vector machine: A case study of mineralized Fe-Ti-Rich gabbroic rocks from the South Eastern desert of Egypt," *Minerals*, vol. 13, no. 6, p. 826, Jun. 2023.

[26] R. Amer, T. Kusky, and A. Ghulam, "Lithological mapping in the central Eastern desert of Egypt using ASTER data," *J. Afr. Earth Sci.*, vol. 56, nos. 2–3, pp. 75–82, Feb. 2010.

[27] S. Gabr, A. Ghulam, and T. Kusky, "Detecting areas of high-potential gold mineralization using ASTER data," *Ore Geol. Rev.*, vol. 38, nos. 1–2, pp. 59–69, Oct. 2010.

[28] Y. Ninomiya and B. Fu, "Thermal infrared multispectral remote sensing of lithology and mineralogy based on spectral properties of materials," *Ore Geol. Rev.*, vol. 108, pp. 54–72, May 2019.

[29] M. Pal and P. M. Mather, "Support vector machines for classification in remote sensing," *Int. J. Remote Sens.*, vol. 26, no. 5, pp. 1007–1011, 2005.

[30] M. J. Cracknell and A. M. Reading, "Geological mapping using remote sensing data: A comparison of five machine learning algorithms, their response to variations in the spatial distribution of training data and the use of explicit spatial information," *Comput. Geosci.*, vol. 63, pp. 22–33, Feb. 2014.

[31] R. Zuo, "Machine learning of mineralization-related geochemical anomalies: A review of potential methods," *Natural Resour. Res.*, vol. 26, no. 4, pp. 457–464, Oct. 2017.

[32] B. W. Heumann, "An object-based classification of mangroves using a hybrid decision tree—Support vector machine approach," *Remote Sens.*, vol. 3, no. 11, pp. 2440–2460, Nov. 2011.

[33] U. Surić, M. Marjanovic, Z. Radić, and B. Abolmasov, "Machine learning based landslide assessment of the belgrade metropolitan area: Pixel resolution effects and a cross-scaling concept," *Eng. Geol.*, vol. 256, pp. 23–38, Jun. 2019.

[34] D. P. Shrestha, A. Saepuloh, and F. van der Meer, "Land cover classification in the tropics, solving the problem of cloud covered areas using topographic parameters," *Int. J. Appl. Earth Observ. Geoinf.*, vol. 77, pp. 84–93, May 2019.

[35] S. Grebby, J. Naden, D. Cunningham, and K. Tansey, "Integrating airborne multispectral imagery and airborne LiDAR data for enhanced lithological mapping in vegetated terrain," *Remote Sens. Environ.*, vol. 115, no. 1, pp. 214–226, Jan. 2011.

[36] R. Latifovic, D. Pouliot, and J. Campbell, "Assessment of convolution neural networks for surficial geology mapping in the South rae geological region, Northwest territories, Canada," *Remote Sens.*, vol. 10, no. 2, p. 307, Feb. 2018.

[37] J. He, J. R. Harris, M. Sawada, and P. Behnia, "A comparison of classification algorithms using Landsat-7 and Landsat-8 data for mapping lithology in Canada's Arctic," *Int. J. Remote Sens.*, vol. 36, no. 8, pp. 2252–2276, Apr. 2015.

[38] S. Kuhn, M. J. Cracknell, and A. M. Reading, "Lithologic mapping using random forests applied to geophysical and remote-sensing data: A demonstration study from the Eastern goldfields of Australia," *Geophysics*, vol. 83, no. 4, pp. B183–B193, Jul. 2018.

[39] W. Ge, Q. Cheng, Y. Tang, L. Jing, and C. Gao, "Lithological classification using sentinel-2A data in the shibanjing ophiolite complex in inner Mongolia, China," *Remote Sens.*, vol. 10, no. 4, p. 638, Apr. 2018.

[40] J. Cardoso-Fernandes, A. C. Teodoro, A. Lima, and E. Roda-Robles, "Semi-automatization of support vector machines to map lithium (Li) bearing pegmatites," *Remote Sens.*, vol. 12, no. 14, p. 2319, Jul. 2020.

[41] I. Bachri, M. Hakdaoui, M. Raji, A. C. Teodoro, and A. Benbouziane, "Machine learning algorithms for automatic lithological mapping using remote sensing data: A case study from Souk Arbaa Sahel, Sidi Ifni inlier, Western Anti-Atlas, Morocco," *ISPRS Int. J. Geo-Inf.*, vol. 8, no. 6, p. 248, May 2019.

[42] H. S. Manap and B. T. San, "Data integration for lithological mapping using machine learning algorithms," *Earth Sci. Informat.*, vol. 15, no. 3, pp. 1841–1859, Sep. 2022.

[43] C. Kumar, S. Chatterjee, T. Oommen, and A. Guha, "Automated lithological mapping by integrating spectral enhancement techniques and machine learning algorithms using AVIRIS-NG hyperspectral data in gold-bearing granite-greenstone rocks in hutti, India," *Int. J. Appl. Earth Observ. Geoinf.*, vol. 86, Apr. 2020, Art. no. 102006.

[44] Y. K. Bentor, "The crustal evolution of the arabo-nubian massif with special reference to the Sinai peninsula," *Precambrian Res.*, vol. 28, no. 1, pp. 1–74, Mar. 1985.

[45] H. A. Hussein, M. A. Hassan, M. A. El-Tahir, and A. Abou-Deif, "Uranium-bearing siliceous veins in younger granites, Eastern desert, Egypt," IAEA, Vienna, Austria, Tech. Rep. IAEA-TECDOC-361, 1986.

[46] H. A. M. Hussein and T. A. Sayyah, "Uranium potential of the younger granites of Egypt," IAEA, Vienna, Austria, Tech. Rep. IAEA-TECDOC-650, 1992.

[47] A. Abu Dief, "The relation between the uranium mineralization and tectonics in some pan-African granite, West of Safaga, Eastern Desert, Egypt," Ph.D. dissertation, Dept. Geol., Assuit Univ., West of Safaga, Eastern Desert, Egypt, 1993.

[48] A. M. Dardier and M. M. El-Galy, "Contribution to the U-th distribution in the older and younger granitoids along Qena-Safaga road," *Egypt. J. Geol.*, vol. 44, no. 1, pp. 55–64, 2000.

[49] S. H. A. E. Nabi, "Evaluation of airborne gamma-ray spectrometric data for the missikat uranium deposit, Eastern desert, Egypt," *Appl. Radiat. Isot.*, vol. 54, no. 3, pp. 497–507, Mar. 2001.

[50] A. A. Ammar and S. I. Rabie, "Schematic relief of the near-surface and deep-seated magnetic basement, using local-power spectra, gabal el-erediya area, Eastern desert, Egypt," *J. Afr. Earth Sci.*, vol. 14, no. 1, pp. 147–152, Jan. 1992.

[51] M. M. El-Mansi, "Petrology, radioactivity and mineralizations of Abu Gerida El-Erediya Area, Eastern Desert, Egypt," Dept. Geol., Cairo Univ., Egypt, 1993.

[52] S. M. Abdallah, "Subsurface geologic studies of el-missikat uranium occurrence, Central Eastern Desert, Egypt," M.Sc. thesis, Dept. Geol., Cairo Univ., Asyut, Egypt, 1998.

[53] A. M. Osman, A. B. Salman, M. M. El-Mansi, I. M. A. Ghani, and S. M. Abdallah, "Mineralogy and uranium distribution in some subsurface sections from el-missikat and el-erediya uranium occurrences, Eastern desert, Egypt," *Delta J. Sci.*, vol. 29, no. 2, pp. 18–38, Dec. 2005.

[54] M. F. Raslan, "Mineralogical and physical separation studies on some radioactive granites from the Eastern Desert, Egypt," Ph.D. dissertation, Dept. Geol., Fac. Sci. Cairo Univ., Giza, Egypt, 2000.

[55] S. M. Abdallah, "Geological and mineralogical studies on some surface and subsurface sections from El-Missikat and El-Erediya uranium occurrences, Central Eastern Desert, Egypt," Ph.D. dissertation, Dept. Geol., Fac. Sci. Ain Shams Univ. Cairo, Giza, Egypt, 2004.

[56] M. A. El-Tahir, "Radioactivity and mineralization of granitic rocks of El-Erediya occurrence, Eastern Desert, Egypt," Ph.D. dissertation, Dept. Geol., Azhar Univ., Egypt, 1985.

[57] A. Abu-Deif, "Geology of uranium mineralization in EL Missikat area, Qena-Safaga road, Eastern Desert, Egypt," M.Sc. thesis, Dept. Geol., Azhar Univ., Cairo, Egypt, 1985.

[58] I. A. El-Kassas and F. S. Bakhit, "Geology of Wadi Alalla-El-Missikat area, Eastern Desert," *Qatar Univ. Sci. Bull.*, vol. 9, pp. 227–244, 1989.

[59] A. M. El-Kammar, N. El-Hazik, M. Mahdi, and N. Aly, "Geochemistry of accessory minerals associated with radioactive mineralisation in the central Eastern desert, Egypt," *J. Afr. Earth Sci.*, vol. 25, no. 2, pp. 237–252, Aug. 1997.

[60] J. K. Osmond, A. A. Dabous, and Y. H. Dawood, "U series age and origin of two secondary uranium deposits, central Eastern desert, Egypt," *Econ. Geol.*, vol. 94, no. 2, pp. 273–280, Apr. 1999.

[61] A. Ahmed, H. S. Abouelnaga, and H. Hasanain, "Distribution of radioelements and its relation to uranium migration, el-erediya exploratory tunnels, central Eastern desert, Egypt," *J. King Abdulaziz Univ.-Earth Sci.*, vol. 13, no. 1, pp. 19–40, 2001.

[62] A. M. El Mezayen, M. A. Heikal, I. K. Abu Zeid, S. A. Omar, M. G. El-Feky, and E. S. R. Lasheen, "Petrography, geochemistry and radioactivity of El-Gidami granitic rocks, central Eastern desert, Egypt," *Al-Azhar Bullet. Sci.*, vol. 9, pp. 25–40, Jul. 2017.

[63] A. A. Ammar, "Application of aerial radiometry of the geology of Wadi El Gdami area," Ph.D. dissertation, Dept. Geol., Fac. Sci., Cairo Univ., Cairo, Egypt, 1973.

[64] F. S. Bakhit, "Geology and radioactive mineralization of G. El Missikat area, Eastern Desert," Ph.D. dissertation, Dept. Geol., Ain Shams Univ., Geiza, Egypt, 1978.

[65] M. A. El Tahir, "Radioactivity and mineralization of granitic rocks of El Erediya occurrence and comparison to El Missikat Rei El-Garra occurrence, Eastern Desert, Egypt," Ph.D. dissertation, Dept. Geol., Azhar Univ., Cairo, Egypt, 1985.

[66] O. Amer, S. Kharbish, A. Maged, and F. Khedr, "Geochemical insight into granite hosted U-rich fluorite, gabal el-erediya area, central Eastern desert, Egypt: REE geochemical and fluid inclusion aspects," *Arabian J. Geosci.*, vol. 14, no. 13, Jul. 2021.

[67] H. H. A. El-Naby, "Genesis of secondary uranium minerals associated with jasperoid veins, el erediya area, Eastern desert, Egypt," *Mineralium Deposita*, vol. 43, no. 8, pp. 933–944, Nov. 2008.

[68] M. Elsaid, H. Aboelkhair, A. Dardier, and E. Hermas, "Investigation of a relation between radiogenic heat production and kinetic surface temperature from multispectral ASTER-TIR data: A case study on elmissikat-eleridiya granites, central Eastern desert, Egypt," *Arabian J. Geosci.*, vol. 7, no. 11, pp. 4615–4628, Nov. 2014.

[69] A. H. Ahmed, *Mineral Deposits and Occurrences in the Arabian–Nubian Shield*. Cham, Switzerland: Springer, 2022.

[70] A. Shebl and M. Hamdy, "Multiscale (microscopic to remote sensing) preliminary exploration of auriferous-uraniferous marbles: A case study from the Egyptian nubian shield," *Sci. Rep.*, vol. 13, no. 1, p. 9173, Jun. 2023.

[71] Z. Hamimi, A. El-Barkooky, J. M. Frías, H. Fritz, and Y. A. El-Rahman, *The Geology of Egypt*. Cham, Switzerland: Springer, 2020.

[72] M. K. Akaad and N. Am, "Geology and lithostratigraphy of the arabian desert orogenic belt of Egypt between latitudes 25O35'and 26O30'N," in *Evol. Miner. Arabian-Nubian Shield. Symp. Abs*, Jeddah, Saudi Arabia, no. 4, 1978, pp. 16–17, doi: 10.1016/0301-9268(78)90063-3.

[73] S. el-Gaby, O. el-Nady, and A. Khudeir, "Tectonic evolution of the basement complex in the central Eastern desert of Egypt," *Geologische Rundschau*, vol. 73, no. 3, pp. 1019–1036, Oct. 1984.

[74] E. Ramly, "A new geological map for the basement rocks in the Eastern and Southwestern Deserts of Egypt," *Ann. Geol. Surv. Egypt*, vol. 2, p. 1, Apr. 1972.

[75] A. A. A. Hussein, M. M. Ali, and M. F. El Ramly, "A proposed new classification of the granites of Egypt," *J. Volcanology Geothermal Res.*, vol. 14, nos. 1–2, pp. 187–198, Oct. 1982.

[76] M. Cuney, P. Le Fort, and Z. X. Wang, "Uranium and thorium geochemistry and mineralogy in the manaslu leucogranite (Nepal, Himalaya)," *Geol. Granites Metallog. Relations*, vol. 2, pp. 853–873, May 1984.

[77] B. Poty et al., "Uranium deposits spatially related to granites in the French part of the Hercynian Orogen," IAEA, Vienna, Austria, Tech. Rep. IAEA-TECDOC-361, 1986, pp. 215–246. [Online]. Available: https://inis.iaea.org/search/search.aspx?orig_q=RN:17039139

[78] M. H. Friedrich and M. Cuney, "Uranium enrichment processes in peraluminous magmatism," in *Proc. Tech. Committee Meeting Uranium Deposits Magmatic Metamorphic Rocks*, IAEA, Vienna, Austria, 1989, pp. 11-35.

[79] M. M. Hassaan et al., "Prognostic exploration of U-F-Au-Mo-W younger granites for geochemical pathfinders, genetic affiliations, and tectonic setting in El-Erediya-El-Missikat province, Eastern desert, Egypt," *Minerals*, vol. 12, no. 5, p. 518, Apr. 2022.

[80] H. A. M. Awad, H. M. H. Zakaly, A. V. Nastavkin, and A. El-Taher, "Radiological implication of the granitoid rocks and their associated jasperoid veins, el-missikat area, central Eastern desert, Egypt," *Int. J. Environ. Anal. Chem.*, vol. 102, no. 19, pp. 8181–8194, Dec. 2022.

[81] I. A. A. El-Leil, A. S. Tolba, S. A. M. Omar, M. G. El-Feky, M. H. Bakiet, and H. A. Awad, "Radioactive mineralization of el-missikat granite; one of most important occurrence, Eastern desert, Egypt," *Int. J. Innov. Sci. Eng. Technol.*, vol. 2, pp. 83–100, May 2015.

[82] A. M. El Mezayen, M. A. Heikal, S. A. Omar, M. G. El-Feky, and E. S. Lasheen, "Petrology, geochemistry and fractional modelling of el gidami neoproterozoic granitic rocks, central Eastern desert, Egypt," *Nat. Sci*, vol. 13, pp. 102–114, May 2015.

[83] F. Ammar, S. Omar, and E. S. El Sawey, "Genetic affiliation of gold and uranium mineralization in el-missikat granite, central Eastern desert, Egypt," *Nucl. Sci. Sci. J.*, vol. 5, no. 1, pp. 33–47, Apr. 2016.

[84] A. Ahmed, H. Abo-Alnaja, and H. Hasanain, "Distribution of radioelements and its relation to uranium migration, el-erediya exploratory tunnels, central Eastern desert, Egypt," *J. King Abdulaziz University-Earth Sci.*, vol. 13, no. 1, pp. 19–40, 2001.

[85] A. Ahmed, H. Abo-Alnaja, and H. Hasanain, "Distribution of radioelements and its relation to uranium migration, el-erediya exploratory tunnels, central Eastern desert Egypt," *J. King Abdulaziz Univ. Sci.*, vol. 5, pp. 19–40, May 2001.

[86] K. Breiter, I. Gnojek, and M. Chlupacova, "Radioactivity patterns–constraints for the magmatic evolution of the two-mica granites in the central moldanubian Pluton," *Vust. Aes. Geol. Ust.*, vol. 73, pp. 301–312, 1998.

[87] N. A. Ahmed, "Comparative study of the accessory heavy minerals in some radioactive rocks of gabal El-missikat and gabal el erediya, Eastern desert. Egypt and their alluvial deposits," M.Sc. thesis, Dept. Geol., Cairo Univ., Giza, Egypt, 1991.

[88] A. Abu-Deif and M. El-Tahir, "A new uranium occurrence, gabal el-missikat prospect, central Eastern desert, Egypt," *J. King Abdulaziz University-Earth Sci.*, vol. 19, no. 1, pp. 85–97, 2008.

[89] I. A. El Kassas, "Radioactivity and geology of wadi atalla area, Eastern desert, Egypt," Ph.D. dissertation, Ain Shams Univ., Cairo, Egypt, 1974.

[90] A. Abu-Deif, S. E. Ammar, and N. A. Mohamed, "Geological and geochemical studies of black silica at el-missikat pluton, central Eastern desert, Egypt," *Proc. Egypt. Acad. Sci.*, vol. 2, pp. 335–346, May 1997.

[91] H. A. Hussein, M. A. El Tahir, and A. Abu-Deif, "Uranium mineralization through exploratory mining work, South qena-safaga midway, Eastern desert, Egypt," in *Proc. 3rd Mining, Petroleum Metall. Conf.*, 1992, pp. 92–105.

[92] E. M. M. Moussa, "Post-collisional A-type granites at al missikat and al aradiya, Eastern desert, Egypt: Geochemical characteristics and REE petrogenetic modeling," in *Proc. 7th Int. Conf. Geochemistry. Alex. Univ., Egypt*, 2006, pp. 1–16.

[93] M. Elsaid, H. Aboelkhair, A. Dardier, E. Hermas, and U. Minoru, "Processing of multispectral ASTER data for mapping alteration minerals zones: As an aid for uranium exploration in elmissikat-eleridiya granites, central Eastern desert, Egypt," *Open Geol. J.*, vol. 8, no. 1, pp. 69–83, Feb. 2014.

[94] E. M. M. Mousa, "Post collisional A-type granites at missikate and Al Aradiya, Central Eastern Desert, Egypt, geochemical charachteristics and REE petrogenetic modeling," in *Proc. 7th Interface Conf. Geochem. Alex. Univ.*, 2008, pp. 1–16.

[95] M. Shalaby, A. Bishta, M. Roz, and M. El-Zalaky, "Integration of geologic and remote sensing studies for the discovery of uranium mineralization in some granite plutons, Eastern desert, Egypt," *J. King Abdulaziz University-Earth Sci.*, vol. 21, no. 1, pp. 1–25, 2010.

[96] M. E. Roz, "Geology and uranium mineralization of Gabal Gattar, North Eastern Desert, Egypt," M.Sc. thesis, Dept. Geol., Fac. Sci. Cairo Univ., Cairo, Egypt, 1994.

[97] M. Y. Meneisy, "On the isotopic dating of the Egyptian basement rocks," *Ann. Geol. Surv. Egypt*, vol. 2, pp. 103–109, Jun. 1972.

[98] A. H. Hashad, "Present status of geochronological data on the Egyptian basement complex," *Precambrian Res.*, vol. 6, no. 1, pp. A24–A25, Jan. 1978.

[99] J. K. Greenberg, "Characteristics and origin of Egyptian younger granites," *GSA Bull.*, vol. 92, no. 5, pp. 749–840, May 1981.

[100] A. El-Sherif, "Mineralogical characterization of the alteration facies at gabal el-missikat area, central Eastern desert, Egypt," *Nucl. Sci. Sci. J.*, vol. 2, no. 1, pp. 1–21, May 2013.

[101] F. Oraby. (1999). *Geologic, Petrographic and Geochemical Studies of Uraniferous Granitoids in El-Garra-El-Gidami Area, Central Eastern Desert*.

[102] T. M. Ibrahim, "Geologic and radioactive studies of the basement-sedimentary contact in the area West Gabal El Missikat, Eastern Desert, Egypt," Ph.D. dissertation, Dept. Geol., Mansoura Univ., Mansoura, Egypt, 2002.

[103] T. E. Amer, T. M. Ibrahim, and S. A. Omar, "Microprobe studies and some rare metals recovery from El-Missikat mineralized shear zone, Eastern Desert, Egypt," in *Proc. 4th Int. Conf. Geol. Afr.*, 2005, pp. 225–238.

[104] P. D. Fullagar, "PAN-African age granites of NorthEastern Africa: New or reworked sialic materials," in *Proc. Symp. Geol. Libya*, Tripoli, Libya, 1980, p. 461.

[105] A. E. El-Kammar, A. H. El-Afandy, T. Nasr, M. Coltorti, and F. Casetta, "Geochemical constraints and uranium potential of the younger granitic rocks in el maghrbia area, central Eastern desert, Egypt," *Acta Geochimica*, vol. 40, no. 4, pp. 623–639, Aug. 2021.

[106] M. Abdel-Hakeem, M. El-Tahir, E. A. Zeid, and H. Rageh, "Genetic implications of Th/U, Th/K, and U/K ratios for u mineralizations: A case study from el-missikat and el-eredіya shear zones, Eastern desert, Egypt," *Geochemical Trans.*, vol. 24, no. 1, p. 3, Oct. 2023.

[107] M. E. Zalaky, "Hyperspectral analysis of aster and Landsat 8 data to characterize el-missikat uranium bearing siliceous veins and their analogy to el-eradiya and gattar granites, Eastern desert, Egypt," *Nucl. Sci. Sci. J.*, vol. 8, no. 1, pp. 99–115, Apr. 2019.

[108] M. Y. Attawiya, "On the geochemistry and genesis of the uranium mineralization in el-missikat area, Egypt," *Ann Geol. Surv.*, vol. 13, pp. 1–15, Jul. 1984.

[109] M. Y. Attawiya, "Mineralogical study of El-ERADYA-1, uranium occurrence, Eastern desert, Egypt," *Arab J. Nucl. Sci. Appl.*, vol. 16, no. 2, pp. 1–26, 1983.

[110] M. F. Raslan, "On the distinction between uranophane and beta-uranophane from some uraniferous granitoids in the Eastern Desert of Egypt," in *Proc. 7th Int. Conf. Geol. Arab World*, 2004, pp. 45–52.

[111] I. Bentahar and M. Raji, "Comparison of Landsat OLI, ASTER, and sentinel 2A data in lithological mapping : A case study of rich area (central high atlas, Morocco)," *Adv. Space Res.*, vol. 67, no. 3, pp. 945–963, Feb. 2021.

[112] A. Singh and A. Harrison, "Standardized principal components," *Int. J. Remote Sens.*, vol. 6, no. 6, pp. 883–896, Jun. 1985.

[113] A. P. Crósta, C. R. De Souza Filho, F. Azevedo, and C. Brodie, "Targeting key alteration minerals in epithermal deposits in patagonia, argentina, using ASTER imagery and principal component analysis," *Int. J. Remote Sens.*, vol. 24, no. 21, pp. 4233–4240, Jan. 2003.

[114] R. P. Gupta, R. K. Tiwari, V. Saini, and N. Srivastava, "A simplified approach for interpreting principal component images," *Adv. Remote Sens.*, vol. 2, no. 2, pp. 111–119, 2013.

[115] T. Pieczonka, T. Bolch, and M. Buchroithner, "Generation and evaluation of multitemporal digital terrain models of the Mt. Everest area from different optical sensors," *ISPRS J. Photogramm. Remote Sens.*, vol. 66, no. 6, pp. 927–940, Nov. 2011.

[116] F. D. van der Meer, H. M. A. van der Werff, and F. J. A. van Ruitenbeek, "Potential of ESA's Sentinel-2 for geological applications," *Remote Sens. Environ.*, vol. 148, pp. 124–133, May 2014.

[117] A. Beiranvand Pour et al., "Application of multi-sensor satellite data for exploration of Zn–Pb sulfide mineralization in the franklinian basin, North Greenland," *Remote Sens.*, vol. 10, no. 8, p. 1186, Jul. 2018.

[118] J. Cardoso-Fernandes, A. C. Teodoro, and A. Lima, "Remote sensing data in lithium (Li) exploration: A new approach for the detection of li-bearing pegmatites," *Int. J. Appl. Earth Observ. Geoinf.*, vol. 76, pp. 10–25, Apr. 2019.

[119] Z. Hamimi, W. Hagag, S. Kamh, and A. El-Araby, "Application of remote-sensing techniques in geological and structural mapping of atalla shear zone and environs, central Eastern desert, Egypt," *Arabian J. Geosci.*, vol. 13, no. 11, pp. 1–27, Jun. 2020.

[120] M. Abd El-Wahed, B. Zoheir, A. B. Pour, and S. Kamh, "Shear-related gold ores in the wadi hodein shear belt, South Eastern desert of Egypt: Analysis of remote sensing, field and structural data," *Minerals*, vol. 11, no. 5, p. 474, Apr. 2021.

[121] N. K. Libeesh et al., "Multispectral remote sensing for determination the ultra-mafic complexes distribution and their applications in reducing the equivalent dose from the radioactive wastes," *Eur. Phys. J. Plus*, vol. 137, no. 2, p. 267, Feb. 2022.

[122] J. Elith, J. R. Leathwick, and T. Hastie, "A working guide to boosted regression trees," *J. Animal Ecol.*, vol. 77, no. 4, pp. 802–813, Jul. 2008.

[123] S. M. Hassan, M. A. S. Youssef, S. S. Gabr, and M. F. Sadek, "Radioactive mineralization detection using remote sensing and airborne gamma-ray spectrometry at wadi al-miyah area, central Eastern desert, Egypt," *Egyptian J. Remote Sens. Space Sci.*, vol. 25, no. 1, pp. 37–53, Feb. 2022.

[124] M. Abrams and S. J. Hook, "Simulated aster data for geologic studies," *IEEE Trans. Geosci. Remote Sens.*, vol. 33, no. 3, pp. 692–699, May 1995.

[125] S. D. Khan, K. Mahmood, and J. F. Casey, "Mapping of muslim bagh ophiolite complex (Pakistan) using new remote sensing, and field data," *J. Asian Earth Sci.*, vol. 30, no. 2, pp. 333–343, Apr. 2007.

[126] A. El Atillah, Z. E. A. El Morjani, and M. Souhassou, "Use of the sentinel-2A multispectral image for litho-structural and alteration mapping in al Glo'a map sheet (1/50,000) (Bou Azzer–El graara inlier, central anti-atlas, Morocco)," *Artif. Satell.*, vol. 54, no. 3, pp. 73–96, Sep. 2019.

[127] M. Khaleghi, "Synergetic use of the sentinel-2, ASTER, and Landsat-8 data for hydrothermal alteration and iron oxide minerals mapping in a mine scale," *Acta Geodynamica Geomaterialia*, vol. 17, pp. 311–328, Aug. 2020.

[128] A. Sheikhrahimi, A. B. Pour, B. Pradhan, and B. Zoheir, "Mapping hydrothermal alteration zones and lineaments associated with orogenic gold mineralization using ASTER data: A case study from the sanandaj-sirjan zone, Iran," *Adv. Space Res.*, vol. 63, no. 10, pp. 3315–3332, May 2019.

[129] A. B. Pour and M. Hashim, "Identification of hydrothermal alteration minerals for exploring of porphyry copper deposit using ASTER data, SE Iran," *J. Asian Earth Sci.*, vol. 42, no. 6, pp. 1309–1323, Nov. 2011.

[130] B. Zoheir, M. A. El-Wahed, A. B. Pour, and A. Abdelnasser, "Orogenic gold in transpression and transtension zones: Field and remote sensing studies of the Barramiya–Mueilha sector, Egypt," *Remote Sens.*, vol. 11, no. 18, p. 2122, Sep. 2019.
[131] A. Hyvärinen, "Independent component analysis: Recent advances," *Phil. Trans. Roy. Soc. A, Math., Phys. Eng. Sci.*, vol. 371, no. 1984, Feb. 2013, Art. no. 20110534.
[132] C. S. Bravo and A. Herrero de Egaña Espinosa de los Monteros, "The influences of the downsizing strategy on business structures," *Rev. Bus. Manage.*, vol. 19, no. 63, pp. 118–132, Feb. 2017.
[133] X.-Y. Zeng and Y.-W. Chen, "Independent component analysis and its application to classification of high-resolution remote sensing images," in *Studies in Computational Intelligence*. Cham, Switzerland: Springer, 2014, pp. 57–81.
[134] C. H. Chen and X. Zhang, "Independent component analysis for remote sensing study," in *Proc. EUROPTO Conf. Image Signal Process. Remote Sens. V*, Florence, Italy, 1999, pp. 150–158.
[135] A. B. Pour, M. Hashim, J. K. Hong, and Y. Park, "Lithological and alteration mineral mapping in poorly exposed lithologies using Landsat-8 and ASTER satellite data: North-Eastern Graham land, Antarctic peninsula," *Ore Geol. Rev.*, vol. 108, pp. 112–133, May 2019.
[136] A. Shebl, M. Abdellatif, M. Hissen, M. Ibrahim Abdelaziz, and Á. Csámer, "Lithological mapping enhancement by integrating sentinel 2 and gamma-ray data utilizing support vector machine: A case study from Egypt," *Int. J. Appl. Earth Observ. Geoinf.*, vol. 105, Dec. 2021, Art. no. 102619.
[137] X. Jia and J. A. Richards, "Segmented principal components transformation for efficient hyperspectral remote-sensing image display and classification," *IEEE Trans. Geosci. Remote Sens.*, vol. 37, no. 1, pp. 538–542, Jan. 1999.
[138] N. Agrawal, H. Govil, S. Chatterjee, G. Mishra, and S. Mukherjee, "Evaluation of machine learning techniques with AVIRIS-NG dataset in the identification and mapping of minerals," *Adv. Space Res.*, vol. 73, no. 2, pp. 1517–1534, Jan. 2024.
[139] A. Guha, S. Mondal, S. Chatterjee, and K. V. Kumar, "Airborne imaging spectroscopy of igneous layered complex and their mapping using different spectral enhancement conjugated support vector machine models," *Geocarto Int.*, vol. 37, no. 2, pp. 349–365, Jan. 2022.
[140] A. M. Youssef, B. Pradhan, A. Dikshit, and A. M. Mahdi, "Comparative study of convolutional neural network (CNN) and support vector machine (SVM) for flood susceptibility mapping: A case study at ras gharib, red sea, Egypt," *Geocarto Int.*, vol. 37, no. 26, pp. 11088–11115, Dec. 2022.
[141] T. Kavzoglu and I. Colkesen, "A kernel functions analysis for support vector machines for land cover classification," *Int. J. Appl. Earth Observ. Geoinf.*, vol. 11, no. 5, pp. 352–359, Oct. 2009.
[142] V. G. Oommen, M. Knowles, and I. Zhao, "Should health service managers embrace open plan work environments?: A review," *Asia Pacific J. Heal. Manag.*, vol. 3, no. 2, pp. 37–43, 2008.
[143] P. H. Sherrod, "Classification and regression trees and support vector machines for predictive modeling and forecasting," DTREG Program Manual, 2003, pp. 281–295.
[144] C. Huang, L. S. Davis, and J. R. G. Townshend, "An assessment of support vector machines for land cover classification," *Int. J. Remote Sens.*, vol. 23, no. 4, pp. 725–749, Jan. 2002.
[145] B. Dixon and N. Candade, "Multispectral landuse classification using neural networks and support vector machines: One or the other, or both?" *Int. J. Remote Sens.*, vol. 29, no. 4, pp. 1185–1206, Feb. 2008.
[146] J. C. Yao et al., "One hundred years after 'Carcinoid': Epidemiology of and prognostic factors for neuroendocrine tumors in 35,825 cases in the United States," *J. Clin. Oncol.*, vol. 26, no. 18, pp. 3063–3072, Jun. 2008.
[147] G. M. Foody, "RVM-based multi-class classification of remotely sensed data," *Int. J. Remote Sens.*, vol. 29, no. 6, pp. 1817–1823, Mar. 2008.
[148] M. F. Raslan, "Mineralogical and geochemical characteristics of uranium-rich fluorite in El-Missikat mineralized granite, Central Eastern Desert, Egypt," *Geologija*, vol. 52, no. 2, pp. 213–220, 2009.
[149] H. A. Awad, H. M. H. Zakaly, A. V. Nastavkin, A. M. El Tohamy, and A. El-Taher, "Radioactive mineralizations on granitic rocks and silica veins on shear zone of el-missikat area, central Eastern desert, Egypt," *Appl. Radiat. Isot.*, vol. 168, Feb. 2021, Art. no. 109493.

Aya S. Shereif received the B.Sc. degree in special geology from the Faculty of Science, Department of Geology, Tanta University, Tanta, Egypt, in 2017, and the M.Sc. degree in petrology and mineralogy from Tanta University in 2022. She is currently pursuing the Ph.D. degree with the University of Debrecen, Debrecen, Hungary.

She is an Assistant Lecturer with Tanta University. She is also a geological researcher. Her research interests span a wide range of disciplines within the realm of geology, including petrology, geochemistry, and radioactivity, especially for the radioactive mineralized zones.

Ali Shebl is currently pursuing the Ph.D. degree with the University of Debrecen, Debrecen, Hungary.

He is a Geological and Environmental Remote Sensing Researcher and an Assistant Lecturer with Tanta University, Tanta, Egypt. His research interests include mineral exploration through remote sensing, geophysical data, and machine learning. Throughout his career, he has assumed pivotal roles within diverse research groups spanning four continents.

Abdelhalim Shokry Mahmoud received the Bachelor of Science degree (Hons.) in geology and chemistry and the Master of Science degree in mineralogy, petrology, and ore deposits from Fayoum University, Al-Fayoum, Egypt, in 2007 and 2013, respectively, and the Ph.D. degree from Russian State Geological Prospecting University, Moscow, Russia, in 2020.

In 2009, he began his career as a Demonstrator at the Department of Geology, Faculty of Science, Fayoum University. Following this achievement, he was appointed as a Lecturer at Fayoum University, where he undertook a scientific mission for post-doctoral research in 2022.

Árpád Csámer received the M.Sc. degree in geography from the Lajos Kossuth University, Debrecen, Hungary, in 1999, the B.Sc. degree in environmental engineering from the University of Debrecen, Debrecen, Hungary, in 2013, the M.Sc. degree in earth science engineering with geological engineering specification from the University of Miskolc, Miskolc, Hungary, in 2016, and the Ph.D. degree from the University of Debrecen, Debrecen, Hungary in 2008.

He has been with the Department of Mineralogy and Geology, University of Debrecen, since 2011. He is proficient in geological exploration, analysis, mapping, and modeling methods, including various microscopy techniques, thermal analysis, remote sensing, GIS, and 3-D computer modeling. His scientific interests primarily relate to applied mineral and petrology research, extraterrestrial materials, interdisciplinary mineral research projects, and environmental geology topics. His research interests also cover applying various geostatistical approaches and comprehensive remote sensing, geophysical, and geospatial analyses in lithological classification and ore exploration.